1-1-2016

Quantitative Assessment Of Brain Iron Content As A Function Of Age Using Magnetic Resonance Imaging

Kiarash Ghassaban
Wayne State University,

QUANTITATIVE ASSESSMENT OF BRAIN IRON CONTENT AS A FUNCTION OF AGE USING MAGNETIC RESONANCE IMAGING

by

KIARASH GHASSABAN

THESIS

Submitted to the Graduate School

of Wayne State University,

Detroit, Michigan

in partial fulfillment of the requirements

for the degree of

MASTER OF SCIENCE

2016

MAJOR: BIOMEDICAL ENGINEERING

Approved by:

_____

Advisor Date

DEDICATION

I dedicate this work to my family

Javad Ghassaban

Shabnam Kordrostami

Khashayar Ghassaban

Parmida Ghassaban

ACKNOWLEDGEMENTS

First and most importantly, I would like to thank my family from the deepest part of my heart. My parents, my grandparents and my siblings have always been there for me throughout my study here in the United States, even though they are thousands of miles away. I definitely would not make it this far, if it was not for their prayers, love and support.

I would also like to express my sincere appreciation to my mentor and advisor, Prof. E. Mark Haacke, who provided me with an outstanding opportunity to pursue my graduate-level education under his supervision. Despite his extremely busy schedule, he always managed to make time for his students and give them new challenges and ideas. As one of the research pioneers in the field of MRI, working under his guidance has always been a privilege for me.

I want to thank all the students, faculty and staff at Magnetic Resonance Research Facility (MRRF) group at Wayne State University; many thanks to Dr. Jaladhar Neelavalli for teaching us the fundamentals of MRI physics, to Mrs. Lisa Brownschidle for her help and patience in administrative affairs, and especially to Dr. Charbel Habib for all his constant support and advice over the past two years; I have learned so much from our long discussions with Dr. Habib and I am very grateful for that.

I would also like to thank all the staff at Magnetic Resonance Innovations who helped me handle different research projects; Mr. David Utriainen, Mr. Sean Sethi, Mr. Paul Kokeny, and especially Mrs. Rachel Martis-Laze. It has been an honor working alongside all of them.

Last but not least, I would like to thank all my friends, here and back home, for all their support and positive vibes. Despite all the fun moments we shared, they have always been there for me through thick and thin.

TABLE OF CONTENTS

LIST OF FIGURES

LIST OF TABLES

ABBREVIATION LIST

AD	Alzheimer's Disease
ADC	Analog to Digital Convertor
BBB	Blood Brain Barrier
BW	Bandwidth
CMB	Cerebral Micro-Bleeds
CN	Caudate Nucleus
CT	Computed Tomography
DN	Dentate Nucleus
EMF	Electromotive Force
FA	Flip Angle
FID	Free Induction Decay
FLAIR	Fluid Attenuation Inversion Recovery
GBCA	Gadolinium-Based Contrast Agents
GM	Gray Matter
GP	Globus Pallidus
GRE	Gradient Recalled Echo
HPF	High Pass Filter
ICPMS	Inductively Coupled Plasma Mass Spectrometry
MRI	Magnetic Resonance Imaging
MS	Multiple Sclerosis
PCC	Pearson Correlation Coefficient
PD	Parkinson's Disease
PET	Positron Emission Tomography
PT	Pulvinar Thalamus
PUT	Putamen
QSM	Quantitative Susceptibility Mapping
RF	Radiofrequency
RN	Red Nucleus

ROI	Region of Interest
RRMS	Relapsing-Remitting Multiple Sclerosis
SE	Spin Echo
SHARP	Sophisticated Harmonic Artifact Reduction for Phase
SN	Substantia Nigra
SWI	Susceptibility Weighted Imaging
T1W	T1-Weighted
T2W	T2-Weighted
TBI	Traumatic Brain Injury
TE	Echo Time
THA	Thalamus
TR	Repetition Time
WM	White Matter
XRF	X-Ray Fluorescence

Chapter One

1 Introduction

In this chapter, a general background will be given on the importance of MR and the motivation behind this work to use it in monitoring iron content, which then will be followed by an overview of the chapters discussed in this thesis.

1.1 Background and Project Motivation

Magnetic Resonance Imaging (MRI) is a non-invasive imaging technique which is now widely used in the clinical setting. As opposed to other common imaging modalities such as Computed Tomography (CT), Positron Emission Tomography (PET) and X-Ray imaging, ionizing radiation is not used in MRI scans, making it a perfect choice to do multiple scans of the same subject, especially in longitudinal studies.

Basically, MRI scans output two different types of data, known as magnitude and phase images, from which a variety of contrast mechanisms can be extracted (by altering the sequence parameters), to image soft tissues. Susceptibility Weighted Imaging (SWI) is one of the recently developed contrasts which is widely used in diagnostic applications (Haacke et al. 2004). By combining magnitude and phase information, SWI is sensitive to the presence of deoxyhemoglobin (i.e. veins), iron accumulation in brain structures as well as micro-hemorrhages, and calcium deposition (Haacke, Reichenbach, and ebrary Inc. 2011). However, since SWI relies on the phase information which is in fact dependent on structural orientation, it can result in potential errors in visualizing veins and cerebral micro-bleeds (CMBs) as well as quantifying iron and calcium content.

Quantitative Susceptibility Mapping (QSM) is a post-processed technique which reconstructs actual magnetic susceptibility distribution, as a source of local phase shifts, from original SWI phase data (Haacke et al. 2015). With QSM being sensitive to tissue magnetic properties, paramagnetic (e.g. deoxyhemoglobin and iron storage) and diamagnetic (e.g. calcium and myelin content) substances can be visualized and quantified with higher accuracy and reliability.

Iron, as the most abundant transition metal present in the human brain, plays a prominent role in a variety of biological processes (Haacke et al. 2007). The temporal distribution of brain iron levels changes as a function of age in healthy people (Li et al. 2014). Moreover, high levels of iron deposition in neurodegenerative diseases, such as Multiple Sclerosis (MS) (Khalil et al. 2011), Alzheimer's Disease (AD) (Antharam et al. 2012), and Parkinson's Disease (PD) (Popescu et al. 2009), have made researchers investigate iron-related interactions over the past two decades through different cross-sectional and longitudinal studies.

With respect to the fact that a sensitive and robust *in vivo* iron-age baseline is required (with a subsequent goal of assessing abnormal iron content), and also given that iron tends to show paramagnetic behavior, QSM has been chosen in this thesis (over other common techniques such as phase and R2*) to establish such a quantitative susceptibility-age baseline in the normal aging brain.

1.2 Thesis Outline

In chapter two, the basic physics of MR signal acquisition will be reviewed, followed by a detailed discussion on the most commonly used sequence, gradient recalled echo (GRE),

which is the underlying sequence in SWI image acquisition scheme. Finally, the concept of magnetic susceptibility and the general algorithm through which the susceptibility distribution (i.e. QSM) is extracted from the SWI phase data will be discussed.

In chapter three, a literature review will be given on the importance of iron physiology and pathophysiology in cases of deviated iron levels in the human body, and especially in the brain. Different types of heme- and non-heme iron and their spatial and temporal distribution in the normal brain will be reviewed based on the literature. In the end, different MR magnitude and phase-dependent iron quantification techniques will be discussed in detail.

In chapter four (a paper published in JMRI), global and regional (i.e. high iron content region) analyses of magnetic susceptibility changes are used to establish the iron-age baseline by using QSM maps of 174 healthy subjects in seven basal ganglia and midbrain structures. The global analysis is validated by being compared to another similar study (Li et al. 2014). Afterwards, linear regression models in both analyses were compared to each other. Finally, by comparing to a cadaver brain study (Hallgren and Sourander 1958), the actual iron concentration-susceptibility correlation is investigated.

According to recent literature over the past few years, due to the confirmed presence of gadolinium-based contrast agents (GBCAs) in dentate nuclei of patients who underwent multiple administrations of contrast agents, and given that linear contrast agents are paramagnetic, the main focus of chapter five is to establish global and regional susceptibility-age baselines of the dentate nucleus using QSM maps of 81 healthy controls. Similar to chapter four, the global analysis is validated by comparing it to Li *et al.*'s study (Li et al. 2014) as well as being compared to the regional analysis in order to assess the linearity of susceptibility changes as a function of age.

Finally, in chapter six, a summary of this thesis will be given along with the conclusions and some potential future directions.

Chapter Two

2 Fundamentals of Gradient Echo Imaging, Phase and Magnetic Susceptibility Quantification

In this chapter, a quick overview of how MRI magnitude and phase signal are acquired through gradient echo imaging (GRE) sequence will be discussed, followed by the basic concepts of magnetic susceptibility and subsequent local phase shifts with their effects on the final MR parameters. In the end, with the main purpose of quantifying magnetic properties of tissues, a general description of quantitative susceptibility mapping (QSM) fundamentals will be given.

2.1 MR Signal Acquisition

From the basics of nuclear physics, we know that in the presence of an external magnetic field ($\vec{B}$), if a typical particle has a nonzero unpaired spin element left (±1/2), the remaining spin will rotate about the direction of the magnetic field. In a right-handed system, the speed with which the spin precess around the magnetic field, also called "precession frequency" or "Larmor frequency" can be defined as (Haacke, Reichenbach, and ebrary Inc. 2011):

$$\vec{\omega} = -\gamma.\vec{B} \tag{2.1}$$

Where γ is the gyromagnetic ratio of the particle[1] and $\vec{\omega}$ is the angular precession frequency. Since the water content makes a major proportion of the human body components, proton

[1] γ is unique for each magnetized particle. For proton, the gyromagnetic ratio is 2.68×10^{8} rad/s/T.

(present in the ^{1}H hydrogen nucleus with the spin value of +1/2) is the most important source of nuclear interactions of the body tissues when exposed to an external magnetic field.

2.1.1 Ideal Signal Formation

In an "isochromat" of spins (i.e. where a group of many spins are exposed to an approximately constant magnetic field), the sum of magnetic vectors, known as the net magnetization ($\vec{M}$) can be calculated through the Bloch equation (Haacke 1999):

$$\frac{d\vec{M}}{dt} = \gamma\vec{M} \times B_0\hat{z} \tag{2.2}$$

Where B_0 is the external magnetic field applied along $\vec{z}$, also known as longitudinal direction. After separating the parallel and perpendicular (transverse) components of the magnetization change, equation (2.2) results in:

$$\frac{d\overrightarrow{M_z}}{dt} = 0 \tag{2.3}$$

$$\frac{d\overrightarrow{M_\perp}}{dt} = \gamma\overrightarrow{M_\perp} \times B_0\hat{z} \tag{2.4}$$

Based on equation (2.4), the time-varying $\overrightarrow{M_\perp}$ (or $\overrightarrow{M_{xy}}$) only occurs when the net magnetization has a transverse component, which does not happen under normal conditions. In order to detect the signal originated from the magnetization process, at a given external magnetic field B_0, a radiofrequency (RF) pulse in "resonance" with the proton Larmor frequency is applied to the whole spin isochromat, tipping it away from the longitudinal direction and towards the transverse x-y plane. Depending on the degree to which the magnetization gets tipped (i.e. "flip angle"), the magnitude of $\overrightarrow{M_{xy}}$ is defined. By rotating

$\overrightarrow{M_{xy}}$ around B_0, a varying flux is induced in a "receiving coil" in front of the imaginary transverse plane which then creates an electromotive force (EMF) under Faraday's law. The origin of the potentially detectable MR signal is this electrical current created from EMF, which then converts to the image format (Haacke 1999).

However, one fact to keep in mind is that the discussion above holds only under ideal conditions in which there is neither an interaction among the spins nor between the spins and the surrounding "lattice".

2.1.2 MR Signal Affected by Relaxation Times

Under realistic circumstances, spins interact with each other as well as the lattice. Regarding the latter, after applying the RF pulse and changing the magnetization orientation, the longitudinal magnetization M_z start to recover to its original position (i.e. aligned with B_0 and along the z direction). The time constant during which the longitudinal magnetization gets back to its equilibrium level (i.e. $M_z = M_0$) is called "spin-lattice relaxation time", also known as T1 (Haacke 1999). Each tissue has its own T1 which is usually determined by experiment. By taking the T1 effect into consideration, after applying the RF pulse, equation (2.3) becomes:

$$\frac{dM_z}{dt} = \frac{1}{T1}(M_0 - M_z) \tag{2.5}$$

Which after solving for the equation yields:

$$M_z(t) = M_z(0)e^{-t/T1} + M_0(1 - e^{-t/T1}) \tag{2.6}$$

On the other hand, due to the subtle variations in the local magnetic field experienced by the spins of a spin isochromat which leads to their different precession frequency, the spins start to dephase from each other. Since the net magnetization is the vector sum of all individual magnetizations, M_{xy} starts to decrease as well. The characteristic time constant during which the transverse magnetization decreases back to its equilibrium level (i.e. $M_{xy} = 0$) is called "spin-spin relaxation time", also known as T2 (Haacke 1999) (See Figure 2.1).

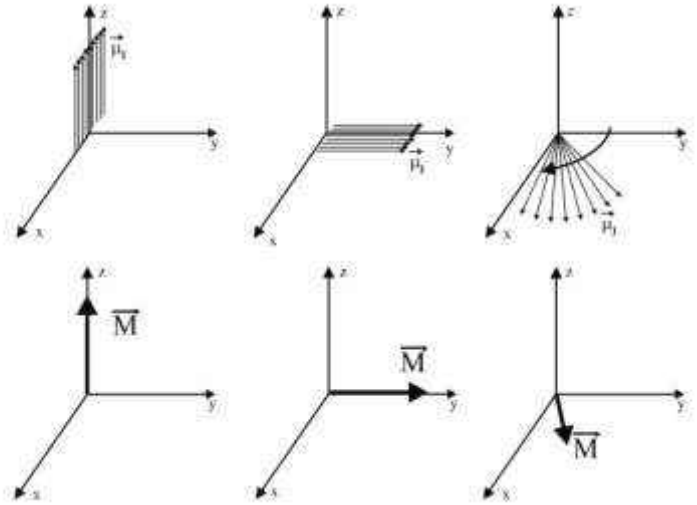

Figure 2.1 Illustration of the T2 effect on a set of spins. The upper row shows a spin isochromat after being exposed to a 90º RF excitation which is tipped along the y direction and then dephases because of spin-spin interactions. The lower row shows the same effect in the form of the net transverse magnetization. If the T1 effect was also accounted for, the vector $\overrightarrow{\boldsymbol{M}}$ at the bottom right would be shorter.[2]

After taking the T2 effect into account, equation (2.4) becomes:

$$\frac{d\overrightarrow{M_{\perp}}}{dt} = \gamma\overrightarrow{M_{\perp}} \times B_0\hat{z} - \frac{1}{T2}\overrightarrow{M_{\perp}} \tag{2.7}$$

Which then after solving for the equation results in:

[2] Image taken from (Haacke 1999).

$$\overrightarrow{M_{\perp}}(t) = \overrightarrow{M_{\perp}}(0)e^{-t/T2} \tag{2.8}$$

The time-course representation of equations (2.6) and (2.8) along with the simultaneous combined effect of both T1 growth and T2 decay are shown in Figure 2.2.

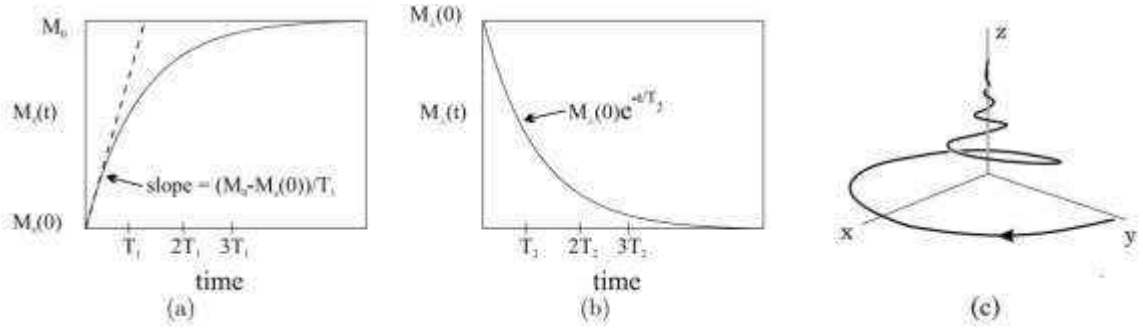

Figure 2.2 Regrowth of the longitudinal magnetization (a) and decay of the transverse magnetization (b) after applying the RF pulse showing the effects of T1 and T2 relaxation times, respectively. The combined effect is visualized as a typical trajectory of the tip of the magnetization $\vec{\boldsymbol{M}}(\boldsymbol{t})$ in (c).[3]

The plot in (b) shows the profile of the signal in the rotating frame.[4] The actual signal profile, called Free Induction Decay (FID), oscillates with an angular Larmor frequency of ω_0 in the laboratory frame. In other words, the actual detected signal in the laboratory frame is defined as:

$$S(t) = S_0\, e^{-\frac{t}{T2}} \sin(\omega_0 t) \tag{2.9}$$

In addition to the mutual spin-spin interactions which lead to the intrinsic T2 decay, there is another source of dephasing which initially stems from external magnetic field (B_0) global inhomogeneities, known as T2'. As a result, the combined time constant associated with the decay of the transverse magnetization, known as T2*, is defined as:

---

[3] Image taken from (Haacke 1999).
[4] This type of reference frame rotates at the Larmor frequency, making the analyses easier for the observer.

$$\frac{1}{T2^*} = \frac{1}{T2} + \frac{1}{T2'} \tag{2.10}$$

With the inverted forms called “relaxation rates” whose relationship is:

$$R2^* = R2 + R2' \tag{2.11}$$

Therefore, after accounting for the local field heterogeneities, equation (2.9) becomes:

$$S(t) = S_0\, e^{-\frac{t}{T2^*}} \sin(\omega_0 t) \tag{2.12}$$

By applying some specific sequence types called “Spin Echo (SE)” which use an additional 180º RF pulses in a different direction (typically along x axis), the dephasing effects of T2’ is recoverable due to their extrinsic nature. However, to date, T2 decay is generally believed not to be removable by any sequence type.

2.2 Gradient Echo Imaging

With respect to recent technological developments, magnetic fields uniformity have reached reasonably minimum levels, making global B_0 heterogeneities less problematic and the use of time-consuming SE sequences less common in the clinical setting. Consequently, by relying on time-variant switches of magnetic fields, a more efficient concept was introduced, known as Gradient Recalled Echo (GRE) sequence, which has recently become commonly used in almost every MR-oriented research and clinical applications (Haacke, Reichenbach, and ebrary Inc. 2011).

2.2.1 GRE Sequence and Signal Acquisition

With reference to a 1-dimentional example shown in Figure 2.3, GRE sequences use dephasing gradients (Figure 2.3a) to manually make the spins of an isochromat get exposed to

spatially different magnetic fields from what is experienced by another isochromat at a different location. These dephasing gradients are followed by "rephrasing gradients" (Figure 2.3b) to make the spins come back to the same angular frequency, and hence the same phase. This way, an "echo" is created at $t = t_4 - \frac{t_4 - t_3}{2}$ $(t' = 0)$. It is important to note that this echo time only refocuses the dephasing effects stemming from applying the first gradient (-G) and not those originating from tissue susceptibilities, field inhomogeneities, and other sources of phase shifts (Haacke 1999).

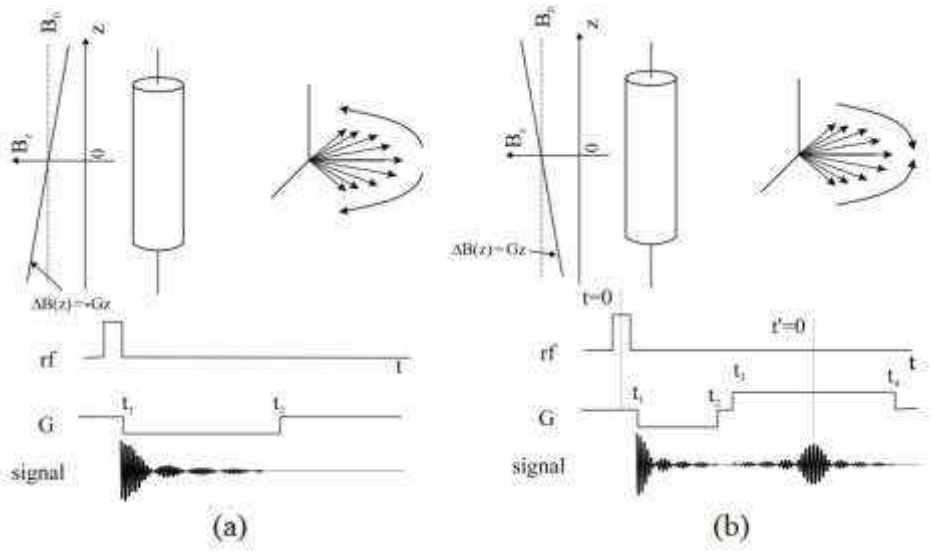

Figure 2.3 A typical 1-D GRE experiment. The cylinders consist of arbitrary spin isochromats located at different locations along z axis. The dephasing part (a) uses a negative gradient -G and the rephrasing part (b) uses a positive gradient +G with the same amplitude.[5]

In case of 2D and 3D GRE acquisition, the concept described in Figure 2.3 should be repeated every TR (repetition time) and as many times as the number of phase encoding direction (typically along y axis) is desired to be. A typical 2D GRE sequence diagram is shown in Figure 2.4. In 3D experiments there is another gradient table added to the slice select

[5] Image taken from (Haacke 1999).

direction ($G_{z,ss}$) with gradient steps accounting for each plane perpendicular to the slice select direction.

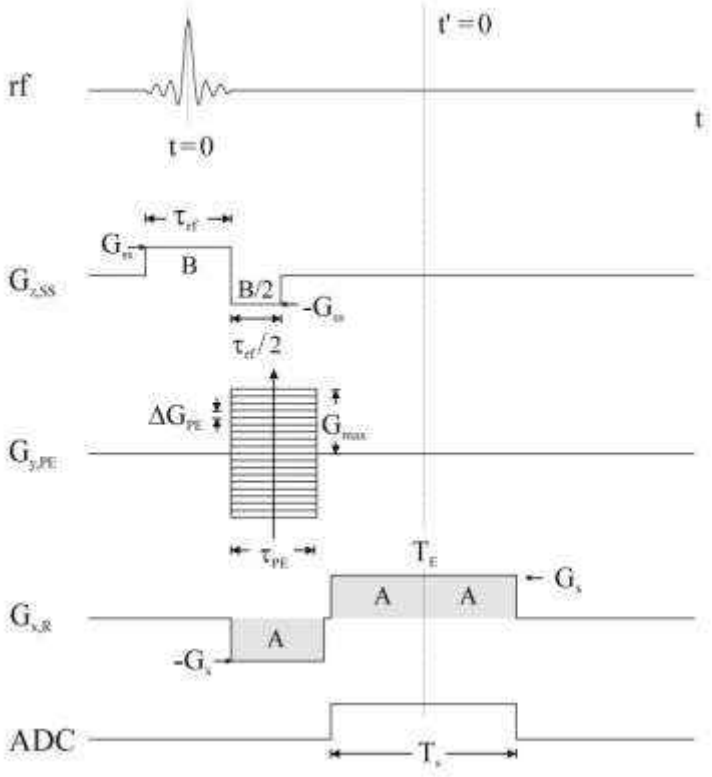

Figure 2.4 A typical 2D GRE experiment where there is a gradient table along the phase encoding (y in this case) direction. The time difference between the gradient steps ΔG_{PE} is TR. Analog to Digital Convertor (ADC) is on when the echo time TE occurs during the sampling time along the readout direction (x in this case).[6]

By taking the role of TR into consideration and the fact that after radiofrequency excitation it takes a variable number of RF pulses for the initial magnetization to reach its equilibrium level[7], M_{ze} can be calculated as:

[6] Image taken from (Haacke 1999).
[7] The number of RF pulses prior to the acquisition can vary from only a few pulses in higher FAs to hundreds of pulses in lower FAs (Haacke 1999).

$$M_{ze} = M_0 \frac{1 - e^{-\frac{TR}{T1}}}{1 - cos\theta . e^{-\frac{TR}{T1}}} \tag{2.13}$$

Where θ is the flip angle and M_{ze} is the equilibrium longitudinal magnetization. By combining equations (2.8) and

(2.13), the transverse magnetization at the time of echo can be given by:

$$Signal \propto M_{xy} = M_0 \frac{1 - e^{-\frac{TR}{T1}}}{1 - cos\theta . e^{-\frac{TR}{T1}}} sin\theta . e^{-\frac{TE}{T2^*}} \tag{2.14}$$

Equation (2.14) is a comprehensive form of the GRE MR signal detected at steady state which accounts for all intrinsic and extrinsic MR parameters. This equation tells us that by manipulating the MR parameters, different contrast mechanisms can be created. For example, at lower flip angles and very short TE, the image is more spin-density weighted, while at higher flip angles when TR is comparable to T1 and with TE being short enough, the image will be more T1-weighted.

2.2.2 Complex MR Signal

From a signal processing perspective, since the magnetization for each individual vector has a unique magnitude and angle when tipped to the transverse plane, then so does the net magnetization. Therefore, the MR signal acquired by a GRE sequence is complex in nature with the magnitude extracted from equation (2.14) and the phase value defined as (Haacke 1999):

$$\phi(\vec{r},t) = \Delta\omega.t = -\gamma.\Delta B(\vec{r}).t \tag{2.15}$$

Where $\Delta B(\vec{r})$ is the field variation experienced by a spin isochromat due to the global and local sources of phase shift such as tissue susceptibility effects, magnetic field inhomogeneities, and chemical shift. Therefore, the complex form of the MR signal can be represented as:

$$S(r,t) = |S(r,t)|e^{i\phi(r,t)} \tag{2.16}$$

Which after accounting for equation (2.14) at the echo time becomes:

$$S(\theta,TE,TR) = S_{xy}(\theta,TE,TR).e^{-i\gamma\Delta B.TE} \tag{2.17}$$

2.2.3 Fourier Transform and K-Space

In a generic form of the simplified 3D GRE sequence (i.e. only with FID effect), assuming that a signal is generated from a set of single spin densities located arbitrarily in a given volume, the signal can be rewritten as:

$$s(t) = \iiint d^3\vec{r}.\rho(\vec{r}).e^{i\phi(\vec{r},t)} = \iiint dxdydz.\rho(x,y,z).e^{i\phi_G(x,y,z,t)} \tag{2.18}$$

Where the phase $\phi_G(x,y,z,t)$ is the sum of accumulated phase in three different directions such that:

$$\phi_G(\vec{r},t) = -\gamma\Delta B(\vec{r})t = -\gamma.G(\vec{r},t)\vec{r}.t \tag{2.19}$$

Here, the amplitudes of gradients are assumed to be spatially and temporally variable. Therefore, by separating the term $G(\vec{r},t)$ in three orthogonal Cartesian coordinates we have:

$$\begin{aligned}\phi_G(x,y,z,t) &= -\gamma.G(\vec{r},t)\vec{r}.t \\ &= -\gamma\left(\int_0^t dt'\,G_x(t')x + \int_0^t dt'\,G_y(t')y \right. \\ &\left. + \int_0^t dt'\,G_z(t')z\right)t\end{aligned} \tag{2.20}$$

As a result, if we define the following "k-space variables" as:

$$k_x(t) = \frac{\gamma}{2\pi}\int_0^t dt'\,G_x(t')x \tag{2.21}$$

$$k_y(t) = \frac{\gamma}{2\pi}\int_0^t dt'\,G_y(t')y \tag{2.22}$$

$$k_z(t) = \frac{\gamma}{2\pi}\int_0^t dt'\,G_z(t')z \tag{2.23}$$

Then equation (2.18) can be rewritten as:

$$s(k_x,k_y,k_z) = \iiint dxdydz.\rho(x,y,z).e^{-2\pi i(k_x x+k_y y+k_z z)} \tag{2.24}$$

Equation (2.24) is technically the Fourier transform of the effective spin density, converting the spatial domain to a corresponding regime, known as k-space domain.

Figure 2.5 shows how k-space is filled following every step described in Figure 2.4. Assuming that the starting point is k_x=k_y=0, after applying each RF pulse, at the corresponding constant phase encoding gradient (G_{PE}), the readout gradient moves the k-space point from $-k_{R,max}$ to $+k_{R,max}$ which makes a line of k-space. After the phase encoding gradient increases by one step (ΔG_{PE}), the same process happens again, but this time the simultaneous change of k_x and k_y sweeps one step higher. The same concept happens at each phase encoding step until the whole k-space is filled with complex sampled points.

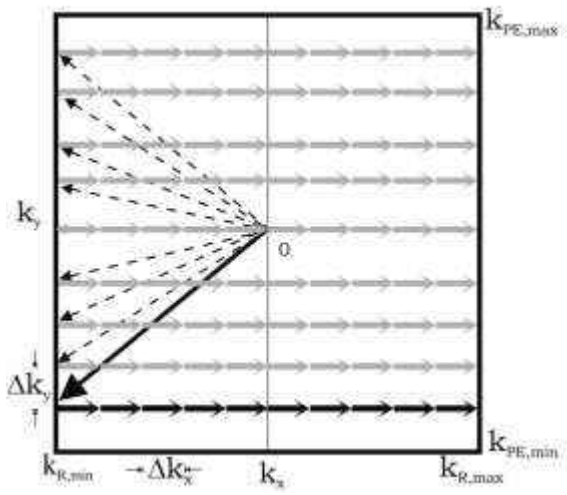

Figure 2.5 A schematic of a 2D k-space filling trajectory corresponding to Figure 2.4. Due to the simultaneous changes of readout and phase encoding gradients as a function of time, k-space filling follows a diagonal trajectory when ΔG_{PE} occurs.

The MRI data-points are typically first acquired in k-space complex domain through real and imaginary channels of the MR scanner. By applying the inverse Fourier transform, original magnitude and phase information are then extracted in spatial domain.

2.2.4 Susceptibility Weighted Imaging

Susceptibility Weighted Imaging (SWI) is a special type of 3D high resolution GRE sequence. In order to minimize the phase-dependent artifacts due to the blood flow effects, SWI is usually fully flow-compensated in all directions by using extra gradient lobes, making the sequence comparatively time-consuming as well (Haacke 1999). The logic behind the flow compensation process is the fact that we are interested in the effects of local susceptibilities, not other contributing factors. A typical 3D SWI sequence diagram has been shown in Figure 2.6.

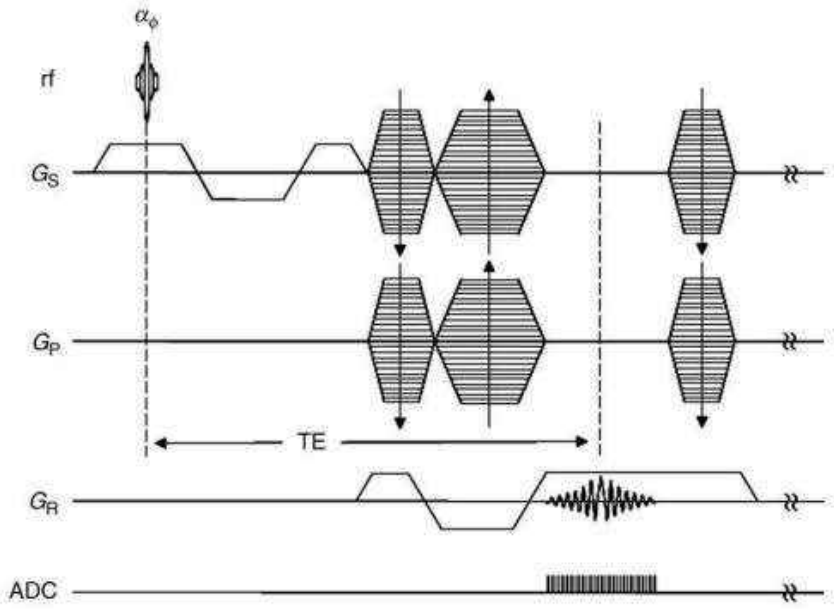

Figure 2.6 A generic form of 3D SWI sequence. Flow compensation with respect to the echo time TE has been applied to readout, slice select, and partition encoding directions.[8]

Going through the same process described in earlier sections of GRE image acquisition, original magnitude and phase images of the SWI sequence can be acquired separately. However, in order to reconstruct the final susceptibility-weighted image, further steps are applied to the original phase image to remove phase wraps and low spatial frequency components, resulting in a weighted mask. The mask then gets multiplied by the original magnitude image to enhance the visualization of signal loss based on the local magnetic susceptibility distribution. The post-processing pipeline of SWI image reconstruction is not the main scope of this thesis. The SWI original phase image, however, which plays a key role in calculating and hence mapping the actual susceptibility values, will be discussed in the following sections.

[8] Image taken from (Haacke, Reichenbach, and ebrary Inc. 2011).

2.3 Magnetic Susceptibility

Magnetic susceptibility (χ) is an intrinsic property of a tissue which manifests its tendency towards being magnetized when exposed to an external magnetic field and how local distribution of the magnetic field can be perturbed by the tissue. Magnetic properties of a typical material can be characterized by three different categories; paramagnetism with positive susceptibility ($\chi > 0$) whose magnetic moments align parallel to the external field, diamagnetism with negative susceptibility ($\chi < 0$) whose magnetic moments align in an opposite direction, and ferromagnetism with very high positive susceptibility ($\chi \gg 1$). Ferromagnetic materials make their own magnetic field, independent of being exposed to external compartments. Iron and calcium are two common paramagnetic and diamagnetic substances, respectively, present in the human body. However, to date, ferromagnetism has not been reported in living tissues in significant amounts (Haacke, Reichenbach, and ebrary Inc. 2011).

A homogeneous external constant magnetic field can be defined as:

$$\overrightarrow{B_0} = \mu_0 \vec{H} \tag{2.25}$$

Where $\vec{H}$ is the vector form of the magnetic flux whose unit is Ampere/meter (A/m) and μ_0 is the absolute permeability of free space ($4\pi \times 10^{-7}$ Tm/A). When an external static field (B_0) passes through an object it induces a magnetization vector ($\vec{M}$) inside the object which also mutually alters the magnetic distribution such that:

$$\vec{B} = \mu_0(\vec{H} + \vec{M}) \tag{2.26}$$

A fundamental equation tells us that the induced magnetization (or permanent in case of ferromagnetism) is related to the flux through magnetic susceptibility:

$$\vec{M} = \chi \vec{H} \tag{2.27}$$

Therefore, using equation (2.27), equation (2.26) can be rewritten as:

$$\vec{B} = \mu_0 (\frac{1+\chi}{\chi}) \vec{M} \tag{2.28}$$

Assuming that we do not deal with permanent magnetization due to ferromagnetism (i.e. $\chi \ll 1$) then equation (2.28) can be simplified to:

$$\vec{B} = \frac{\mu_0}{\chi} \vec{M} \tag{2.29}$$

And therefore:

$$\vec{M} = \frac{1}{\mu_0} \chi \vec{B} \tag{2.30}$$

Equations (2.29) and (2.30) show the relationship between the induced magnetization and perturbed magnetic field inside the exposed object. However, based on the object geometric characteristics such as overall shape and orientation, the induced magnetization can cause field perturbation outside the object as well. With respect to the fact that blood vessels can be modeled by long symmetric cylinders and spheres resemble micro-bleeds and sinuses, these two structures are usually used to study field variations as a function of magnetic susceptibility. Table 2.1 shows susceptibility-dependent field perturbation of these two structures inside and outside the object (Haacke, Reichenbach, and ebrary Inc. 2011).

Table 2.1 Field perturbation inside and outside a long cylinder and a uniform sphere.

	Internal Field Shift	External Field Shift
Sphere	B_0	$B_0 + \frac{\chi B_0}{3} . \frac{a^3}{\lvert\vec{r}\rvert^3} . (3cos^2\theta - 1)$
Cylinder	$B_0 + \frac{\chi B_0}{6} . (3cos^2\theta - 1)$	$B_0 + \frac{\chi B_0}{2} . \frac{a^2}{\lvert\vec{r}\rvert^2} . sin^2\theta cos2\phi$

a: radius of the sphere/cylinder. θ for cylinder: angle between cylinder central axis and B_0. θ for sphere: angle that the perpendicular position vector $\vec{r}$ makes with B_0. ϕ: polar angle between $\vec{r}$ and cylinder axis.

It should be noted, however, that the susceptibility values reported in Table 2.1 are the absolute values in vacuum. If these structures were to be located at a more realistic environment with known susceptibility behavior, the relative susceptibility values ($\Delta\chi$) should be used instead. For example, since the human body is dominated by water content, magnetic susceptibility of water molecules relative to vacuum may be used as a reference to define structural susceptibilities.

2.4 Phase Signal and Susceptibility Mapping

2.4.1 Phase Image Processing

Based on equation (2.15), the phase data at the echo time TE can be written as:

$$\phi(\vec{r}) = -\gamma . \Delta B(\vec{r}) . TE \tag{2.31}$$

Basically, there are two different sources of field variation; first, macroscopic or global sources such as geometric orientation of the structures (e.g. air-tissue and air-bone interface) and intrinsic external field inhomogeneities. Second, microscopic or local sources of variation which are mostly in the form of susceptibility distribution and chemical shift. Overall, the total field distribution can be defined as:

$$\Delta B_{Total} = \Delta B_{External\ Field} + \Delta B_{Chemical\ Shift} + \Delta B_{Global\ Geometry} + \Delta B_{Susceptibility} \quad (2.32)$$

While $\Delta B_{Susceptibility}$ depends on the structural shape and orientation, $\Delta B_{Chemical\ Shift}$ is only dependent on the substance itself and its magnetic properties compared to the water molecules.[9] Due to the fact that we are interested only in investigating susceptibility effects, we have to minimize the effects of other contributing factors present in the total field variation equation, a process known as "background field removal".

One of the problematic issues present in the original phase images is "phase aliasing". This phenomenon occurs when the magnitude and phase images are acquired through real and imaginary channels of the MR scanner. However, because these channels use the polar coordinates to reconstruct magnitude and phase (argument) information of the complex MR signal, the phase value is limited to [-π π] range. As a result, each value higher than π wraps back to –π, and accordingly, any phase value lower than -π wraps back to π. The actual phase value can be calculated as:

$$\phi_{True}(\vec{r}) = \phi_{Measured}(\vec{r}) + 2\pi.n(\vec{r}) \quad (2.33)$$

Where $n(\vec{r})$ is the number of times the pixel-wise phase value has been aliased. Since background field variations have comparatively low spatial frequency, applying a high-pass spatial filter (HPF) is a reliable and robust method to minimize these background field effects. (Wang et al. 2000).

[9] In this thesis, since the focus is on the brain tissue, the local field variation is mostly dominated by the susceptibility distribution.

In a typical homodyne high-pass filter, a Hanning window is located at the center of the k-space and depending on the filter size, only collects low spatial information (i.e. bulk complex data) from the k-space. As shown in equation (2.34) and Figure 2.7, a complex division of the original reconstructed image ($\hat{\rho}$) by the truncated filtered image will then output the high-pass filtered phase image (Liu 2014).

$$arg\left(\hat{\rho}_{HighPass}\right) = arg\left(\frac{\hat{\rho}}{\hat{\rho}_{LowPass}}\right) \tag{2.34}$$

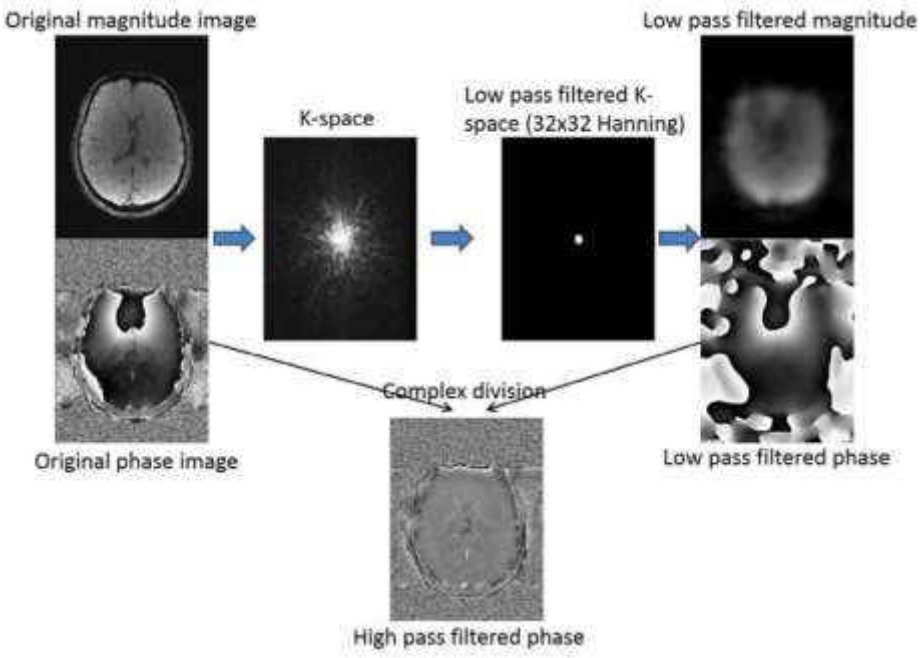

Figure 2.7 General pipeline of a homodyne high-pass filter.

One of the most important advantages of high-pass filtering is its high execution speed and the fact that it does not require any phase unwrapping step, making it a very suitable choice in both research and clinical settings. However, due to the fact that using bigger HPF window size (e.g. 128 × 128) also removes useful low spatial information in larger structures and hence underestimates the contribution of the signal itself, other background field removal

techniques, such as variable high-pass filtering (vHPF) (Haacke et al. 2015) and Sophisticated Harmonic Artifact Reduction for Phase data (SHARP) (Schweser et al. 2011) have been suggested for quantification purposes.

2.4.2 Quantitative Susceptibility Mapping

In a right-handed system, by assuming that the external static field is along the z-axis, equation (2.31) can be rewritten as:

$$\phi(\vec{r}) = -\gamma . \Delta B_z(\vec{r}) . TE \tag{2.35}$$

Where $\Delta B_z(\vec{r})$ can be derived via (Haacke et al. 2015):

$$\Delta B_z(\vec{r}) = \frac{\mu_0}{4\pi} \iiint d^3r' [\frac{3M_z(\overrightarrow{r'})(z-z')^2}{\left|\vec{r}-\overrightarrow{r'}\right|^5} - \frac{M_z(\overrightarrow{r'})}{\left|\vec{r}-\overrightarrow{r'}\right|^3}] \tag{2.36}$$

Which in fact can be reformatted to a convolution:

$$\Delta B_z(\vec{r}) = \mu_0 M_z(\vec{r}) * G(\vec{r}) \tag{2.37}$$

Where $G(\vec{r})$ is called the Green's function and is given by:

$$G(\vec{r}) = \frac{1}{4\pi} \frac{3cos^2\theta - 1}{r^3} \tag{2.38}$$

In which θ is the angle between position vector $\vec{r}$ and the external field direction $\vec{z}$. By incorporating equations (2.29) and (2.37) we can modify equation (2.37) to:

$$\Delta B_z(\vec{r}) = B_0 \chi(\vec{r}) * G(\vec{r}) \tag{2.39}$$

Defined as "Forward Modeling Process", solving for equation (2.37) or (2.39) by using the convolution theorem, leads us to the spatial field variation and hence phase distribution.

However, assuming that we already have the phase information and want to extract the actual susceptibility distribution, we have to come back from the effect (i.e. phase) to the source (i.e. susceptibility) through a technique, known as “Inverse Process”.

The Fourier transform of the Green’s function can be easily calculated as (Haacke et al. 2015):

$$G(\vec{k}) = \begin{cases} \frac{1}{3} - \frac{k_z^2}{k^2}, & k \neq 0 \\ 0, & k = 0 \end{cases} \tag{2.40}$$

Where the k-space components are related via $k^2 = k_x^2 + k_y^2 + k_z^2$. Now by manipulating equation (2.39) and using Fourier transform properties we can derive:

$$\Delta B_z(\vec{r}) = B_0 \,.\, FT^{-1}\{\chi(\vec{k}) \,.\, G(\vec{k})\} \tag{2.41}$$

And hence:

$$\chi(\vec{k}) = \frac{\Delta B_z(\vec{k}).\, G^{-1}(\vec{k})}{B_0} \tag{2.42}$$

And finally, by combining equations (2.42) and (2.35) and the fact that we have access to the original phase information, spatial susceptibility distribution can be derived as:

$$\chi(\vec{r}) = -\frac{FT^{-1}\left(\phi(\vec{k}).\, G^{-1}(\vec{k})\right)}{\gamma.\, B_0\,.\, TE} \tag{2.43}$$

Equation (2.43) is the main formula through which the susceptibility mapping procedure is done. A schematic diagram of quantitative susceptibility mapping (QSM) is shown in Figure 2.8 . It should be noted that brain masks are not a necessary part of the algorithm, but using them enhances image processing speed and accuracy.

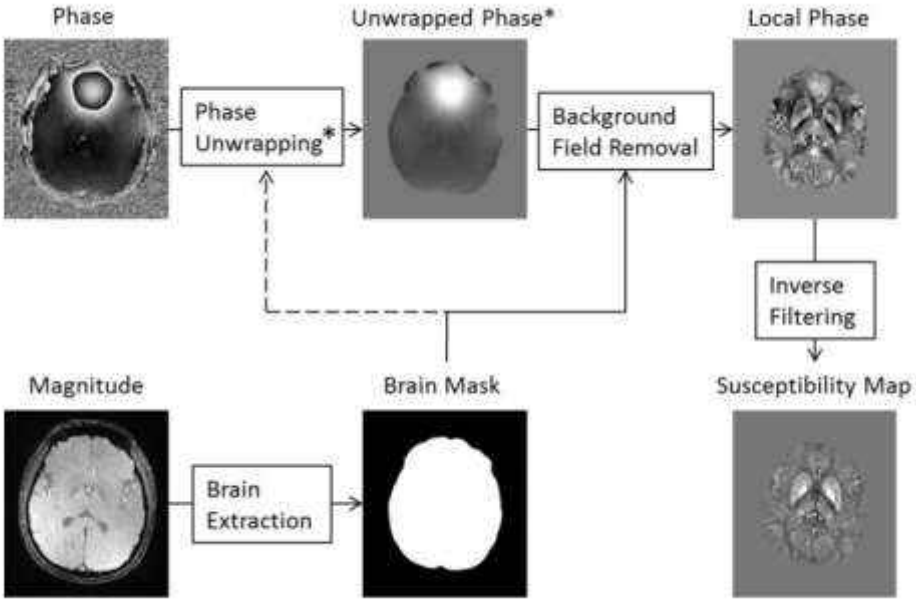

Figure 2.8 Schematic diagram of general QSM post-processing algorithm. *Involvement of the phase unwrapping step depends on the background removal method. Brain extraction step is not mandatory, but enhances reconstruction speed and accuracy.[10]

On the other hand, as seen in equations (2.40) and (2.43), $G^{-1}(\vec{k})$ is not defined in k-space points where the denominator is close to zero, a condition known as "ill-posed problem", which causes a special type of image complication called "streaking artifact". Streaking artifacts have been tried to be dealt with through post-processing techniques, such as truncated k-space (Haacke, Tang, et al. 2010).

In summary, QSM provides the opportunity to not just visualize the presence of iron (paramagnetic) and calcium (diamagnetic) but also the ability to quantify the amount of either substance in the brain. Therefore, since iron is a paramagnetic material having a positive susceptibility, using QSM maps is a proper choice to map the true iron content in the brain. In the next three chapters, brain iron quantification will be discussed in detail.

[10] Image taken from (Liu 2014) with permission.

Chapter Three

3 Brain Iron Physiology and Quantification

3.1 Introduction to Iron Physiology

Iron has long been known for playing key roles in a variety of brain physiologic interactions such as the brain metabolism, neuronal maturation, dopamine production, myelin generation, electron and oxygen transport and so on (Berg and Youdim 2006; Stankiewicz et al. 2007), making it the most important transition metal present in the human brain. Additionally, brain iron levels has been seen to be correlated with normal aging which could also explain pathophysiological interactions in the diseased brain (Hare et al. 2013); For example, elevated iron is associated with a number of brain disorders namely Alzheimer's Disease (AD) (Loef and Walach 2012), Parkinson's Disease (PD) (Ayton et al. 2013), and Multiple Sclerosis (MS) (Habib et al. 2012). Also, based on the literature, iron deficiency is also a sign of some other disorders such as Attention Deficit Hyperactivity Disorder (ADHD) (Cortese et al. 2009) and neurodegeneration in general (Jeong et al. 2011). On the other hand, living organisms in the human body apply different methods to keep the iron homeostasis level and prevent iron overload or deficiency (Ropele et al. 2011).

Basically, there are two general categories of iron forms present in the human body; almost 70% of it is in the form of "heme-iron" (i.e. hemoglobin which is responsible for oxygen transport) and 30% in the form of "non-heme iron" (e.g. deposited in the organs, structures, proteins etc.) (Haacke et al. 2005; Hallgren and Sourander 1958). As the name of "transitional metal" suggests, iron is mostly in the form of Ferric (Fe^{3+}) or Ferrous (Fe^{2+}).

From a chemical point of view, Ferric is comparatively more stable leading to its higher proportion in the human body.

3.2 Different Forms of Iron

Iron is usually stored in a ubiquitous soluble protein called Ferritin, which is naturally produced by living organisms in the body. The major function of ferritin is to make excess iron accumulate in its subunits thereby keeping the iron homeostasis level from changing. Ferritin is a fairy large spherical molecule consisting of 24 sub-units which can store up to 4500 atoms of iron in its central hollow part (see Figure 3.1).

Figure 3.1 Ferritin protein. The hollow section (mineral core) of the molecule can store up to 4500 iron atoms[1]

Hemosiderin is another form of iron storage protein. Unlike ferritin, hemosiderin is an insoluble molecule which is believed to be a fairly immediate product of ferritin denaturation process. This protein could be found in white blood cells and has been seen to be present in comparatively large proportions in diseased brains which are believed to be associated with

[1] Image taken from: https://ilovebiochem1362.wordpress.com/2013/02/14/amino-acids-and-proteins

cerebral hemorrhages (Schenck and Zimmerman 2004). Stroke (Kleinig 2013) and Traumatic Brain Injury (TBI) (Benson et al. 2012) are common clinical examples of hemosiderin with an external appearance of cerebral hemorrhage.

The last type of the normal non-heme iron proteins is called transferrin. As the name suggests, the major role of this molecule is to deliver iron and iron-related products to different parts of the body. Specifically in the brain, transferrin's responsibility is to deliver iron to the brain through the blood brain barrier (BBB) (Haacke et al. 2005). However, since transferrin binds to only two iron atoms, the effect of iron on this molecule is not enough to cause considerable magnetic field variation which makes it practically undetectable via MR methods.

From a distribution standpoint, different types of non-heme iron have been shown to be heterogeneously distributed in different parts of the brain (Haacke et al. 2005). Histochemically investigated, both iron atoms (mostly Fe^{3+}) and ferritin molecules have been reported to be almost equally distributed in gray matter and white matter, while transferrin showed more notable presence in the white matter (Connor et al. 1992). However, in deep gray matter structures, ferritin, as the dominant type of iron, showed variance both spatially and temporally with the highest average values in the Globus Pallidus and the highest age-dependency rate in the Putamen (see chapter 4 for more details). Also, as reported by a famous iron study done by Hallgren and Sourander, the highest concentration of non-heme iron content in the cortical regions was found in the motor cortex followed by occipital cortex and sensory cortex (Hallgren and Sourander 1958).

3.3 Iron in the Aging Brain

Iron deposition in the brain versus normal aging has been investigated for a long time. Back in the 1950s, from a cadaver brain study, Hallgren and Sourander had shown that the brain iron levels change in different parts of the brain as a function of age generally with very low values in infants, followed by an almost exponential increase in the first two decades and a leveling off or a linear trend afterwards (Hallgren and Sourander 1958). These findings have been validated in other studies using *in vivo* MR techniques (see section 3.4) in which the same conclusions have been made (Xu, Wang, and Zhang 2008; Li et al. 2014; Zivadinov et al. 2010). For instance, deep gray matter nuclei showed different exponential and linear trends of iron deposition as a function of age; in a recent study done by Li *et al.,* some structures such as the putamen, the dentate nucleus, and the caudate nucleus have been reported to show an almost linear iron-age increasing behavior across the lifespan, while other nuclei such as the globus pallidus, the red nucleus, and the substantia nigra revealed an exponential growth pattern with higher increase rate in the first two decades followed by an almost constant levels of iron in subsequent decades (Li et al. 2014). However, by using a novel method called "regional high iron content analysis", there are also some new subtle trends revealed in brain iron accumulation as a function of age which was not reported in previous studies (Haacke, Miao, et al. 2010).[2] In general, basal ganglia and brain stem nuclei tend to have higher levels of iron concentration in the elderly, while the thalamic regions and cortical white matter are believed to have more iron storage in younger people (Pfefferbaum et al. 2009). Although iron presence is believed to be mostly dominated by deep gray matter and cerebellar nuclei, a

[2] This concept will be discussed in detail in chapter 4.

recent whole-brain study has shown that in addition to these regions, frontal lobes also tend to build up excessive iron content as a function of age (Acosta-Cabronero et al. 2016).

As seen in the discussion above, the distribution of non-heme brain iron content tends to have a non-homogenous pattern both spatially and temporally.

3.4 MR Techniques for Iron Quantification

As discussed in the previous chapter, MR signal is directly dependent on the concentration of water molecules within a given volume of tissue (i.e. the voxels). On the other hand, as the time goes on, these cohorts tend to build up the complementary phase signal as well. However, the presence of magnetically-known particles alters these important MR signal characteristics which could be useful in subsequent post-processing applications; for example, the abundance of metal elements in the brain has an altering effect on both magnitude and phase information via the relaxivity and susceptibility changes, respectively. Accordingly, these predictable changes make the visualization and quantification of the metal presence feasible *in vivo*.

Since iron is known to be paramagnetic and its presence has been seen to be more prominent in deep gray matter structures (as compared to other metals such as copper, calcium, zinc etc.), the susceptibility-related local field variations in these regions are believed to be due to the iron atoms magnetic effects. To date, there has been a strong interest in quantifying brain iron content using a broad spectrum of MR methods. Brain iron quantification provides potential complementary information about normal iron build up due to the brain maturation process over the lifespan (Hallgren and Sourander 1958; Li et al. 2014) as well as a variety of different iron-related neurodegenerative disease such as

Parkinson's Disease (Barbosa et al. 2015), Multiple Sclerosis (Habib et al. 2012), and Alzheimer's Disease (Langkammer et al. 2014) and also a spectrum of disorders characterized by cerebral hemorrhage, namely, stroke (Kleinig 2013) and traumatic brain injury (Benson et al. 2012). Another useful application of iron quantification is to quantify the levels of deoxyhemoglobin in veins (which also acts as a paramagnetic substance when exposed to external magnetic field) resulting in oxygen saturation measurement which is in fact directly related to cerebral perfusion (Haacke, Tang, et al. 2010).

As mentioned earlier, ferritin and hemosiderin are the only iron storage molecules which are detectable through MR techniques, while transferrin and other iron-related receptors cannot be quantified via MR due to their scattered presence and lower concentrations (Haacke et al. 2005).

The main focus of this thesis will be on quantification of ferritin in cerebrum, cerebellum, and brainstem. In this section, commonly used MR methods with the main emphasis on cerebral iron quantification will be discussed in detail.

3.4.1 T2, T2' and T2* Relaxation Times

As discussed in previous sections, the presence of a paramagnetic material makes the local effective magnetic field deviate from the original orientation which subsequently affects the interaction of spins with each other within a given volume. This phenomenon finally leads to disruptive changes in relaxation rates. In general, spin-spin relaxation rates (R2, R2' and R2* as the inverse forms of T2, T2' and T2*) have been seen to increase as a function of iron content in the brain tissue (Haacke et al. 2005).

Iron as Seen with R2 Changes

It has been shown that the presence of a paramagnetic substance could cause additional stochastic Brownian motion in water molecules of a given exposed tissue which cannot be recovered via spin-echo sequences (Langkammer et al. 2010):

$$R2_{eff} = R2_0 + R2_{diff} \quad (3.1)$$

Where $R2_0$, $R2_{dif}$ and $R2_{eff}$ are the intrinsic tissue relaxation rate under normal conditions, induced positive relaxation time due to the unrecoverable stochastic movement, and the total effective tissue relaxation time, respectively.

This microscopic magnetic phenomenon makes it feasible to keep track of iron content when other sources of field variation are removed at the echo time of the spin-echo (SE) sequence. A positive correlation between R2 and the true iron concentration (μgFe/g wet tissue) in the brain tissue has been reported in several studies both in normal and diseased conditions (Langkammer et al. 2010; Barbosa et al. 2015; Mitsumori, Watanabe, and Takaya 2009). However, there are two major drawbacks with this method; first, the intrinsic $R2_0$ itself changes as a function of magnetic field strength which is expandable to R2* as well (see equation (3.2)) (Yao et al. 2009). Second, the diffusion-related relaxation term in equation (3.1) is relatively small compared to the intrinsic term making $R2_{eff}$ less sensitive to $R2_{diff}$ variation. By taking these two major setbacks into account, one can conclude that although R2 is correlated with iron concentration, it is not accurate enough for iron quantification purposes.

R2' and R2 Techniques*

As pointed out in chapter 2, the general equation between tissue relaxation times is:

$$R2^{*} = R2 + R2' \tag{3.2}$$

where R2' is characterized by all sources of dephasing which can potentially be refocused through a 180º pulse in a spin-echo sequence. The dephasing effect of a given paramagnetic material, such as iron in local field distributions, is much stronger on R2' compared to R2, meaning that both R2' and R2* are more sensitive to iron deposition than R2 (Langkammer et al. 2010). With regard to the MR signal equation discussed in chapter 2, by having at least two echoes in a multi-echo spoiled gradient echo sequence, with given repetition time TR and flip angle θ, an R2* map can be reconstructed easily (e.g. by dividing the two GRE signal intensities in case of having two echoes). R2* has been reported to have a linear correlation with actual iron concentrations in the brain (Langkammer et al. 2010; Stuber et al. 2014). R2*, as a representative MR parameter for the iron content in the brain, has also been shown to be correlated with age in different parts of the brain (Haacke, Miao, et al. 2010; Li et al. 2014). However, just like R2, R2* also varies as a function of external magnetic field due to its dependency on R2. Additionally, since R2* is directly measured from the magnitude information, the signal loss in more magnetically susceptible regions (e.g. air-bone and air-tissue interface) makes it harder to extract accurate R2* values, especially in longer echo times and higher magnetic fields.

3.4.2 Iron as Measured with Phase

The phase information is directly proportional to local magnetic field variations as represented by the following equation:

$$\phi(\vec{r}, TE) = \Delta\omega(\vec{r}).TE = -\gamma.\Delta B(\vec{r}).TE \quad (3.3)$$

where the parameter $\Delta B(\vec{r})$ is an effect of the local magnetic susceptibility present within the tissue of interest which is also a direct measure of any field-inducing material (either diamagnetic or paramagnetic), including iron. Phase is sensitive even to small amounts of iron, making it a potentially better candidate as compared to R2 and R2* techniques, especially when phase information has revealed strong correlations to iron concentrations and age-dependency in the brain (Haacke, Miao, et al. 2010). On the other hand, there are a few limitations with phase as well such as different sources of phase shift other than the iron content (e.g. local and global magnetic field inhomogeneities), limited value range of [-π π] and subsequent wrapping problems when more phase accumulates as well as phase dependency upon object geometry and orientation (Yao et al. 2009). These limitations may raise technical issues when dealing with phase information for quantification purposes which necessitates further post-processing algorithms.

3.4.3 Iron Quantification via QSM

An alternative way to avoid almost all the aforementioned restrictions associated with phase information is to extract and map the source of these uncertainties (i.e. absolute magnetic susceptibility values) via Quantitative Susceptibility Mapping (QSM) (Haacke et al. 2015; Reichenbach et al. 2015).[3] Theoretically, QSM is not dependent on geometric orientation of the structure of interest, echo time, and magnetic field strength which makes it a very suitable candidate to quantify brain iron content (Zheng et al. 2013; Haacke et al. 2015). Table 3.1 summarizes the correlation between the true susceptibility values extracted from

[3] Details of QSM reconstruction are also available in chapter 2.

QSM maps and iron concentration in human brain reported in a recently published paper by Haacke *et al.* (Haacke et al. 2015). Depending on the type of the measured iron and the experiments being *in vivo* or *in vitro*, the slopes were reported differently; Langkammer *et al.* used average QSM susceptibility values of deep gray matter and white matter structures in order to compare them to Inductively Coupled Plasma Mass Spectrometry (ICPMS) results from cadaver brains (Langkammer, Schweser, et al. 2012), while Zheng *et al.* compared QSM susceptibility values with X-Ray Fluorescence (XRF) maps in a pixel-by-pixel manner (Zheng et al. 2013). The slope from this *in vitro* study was similar to what Langkammer *et al.* had reported before. On the other hand, depending on the techniques, the *in vivo* studies did not seem to be as consistent; by comparing susceptibility values to Hallgren and Sourander's actual iron concentration measurements, Haacke *et al.* came up with a slope of 0.59 ppb/µgFe/g tissue[4] which is comparable to Shmulei *et al.* and Wharton *et al.*'s reported slopes (Wharton and Bowtell 2010; Shmueli et al. 2009), whereas their correlations were smaller than those investigated in Schweser *et al.*'s work (Schweser et al. 2011). However, as discussed in chapter four, by investigating 174 healthy subjects and comparing them to Hallgren and Sourander's iron measurements, it was shown that the slope between the magnetic susceptibility and iron concentration is roughly 1 ppb/µgFe/g tissue, which is consistent with other phantom and cadaver brain studies as well.

More detailed discussion regarding the correlation of the brain structures' susceptibilities with respect to normal aging as well as iron concentration will be given in the following chapter.

---

[4] http://www.ismrm.org/12/WK_Neuro1.htm.

Table 3.1 Correlation between susceptibility mapping and iron concentration (Haacke et al. 2015). [1]

Authors	Correlation Slope [a]	Structures [b]	Background Removal Technique	QSM Method [c]	Myelin Correction	Field Strength	Sample	Iron
Zheng *et al* (2013)	1.11	N.A.	Quadratic Fitting	Forward Fitting	N.A.	3 T	Ferritin	ICPMS
Zheng *et al* (2013)	1.10	N.A.	Quadratic Fitting	Forward Fitting	N.A.	3 T	Ferritin	XRF
Zheng *et al* (2013)	0.80	GP, PUT, CN	SHARP	TKD (SO)	No	3 T	MS Cadaveric Brain (fixed)	XRF
Haacke *et al.* (2012)	0.59	GP, PUT, CN	SHARP	TKD (SO)	No	3 T	*In vivo* brains	H&S [d]
Shmueli *et al.* (2009)	0.56	PUT, RN, SN	Polynomial Fitting	TKD (SO)	No	7 T	*In vivo* brain	H&S
Wharton *et al.* (2010)	0.75/0.6	GP, SN, RN, PUT, CN, TH, GM	Simulated geometric effect + fitting	TKD (MO/SO)	No	7 T	*In vivo* brains	H&S
Langkammer *et al.* (2012a)	0.89	GP, PUT, CN, TH	SHARP	HEIDI (SO)	No	3 T	Unfixed Cadaveric Brains	ICPMS
Schweser *et al.* (2011)	1.30	GP, SN, DN, PUT, CN, TH, WM, GM	SHARP	MO Regularization	Yes	3 T	*In vivo* brains	H&S

[a] The unit of the slope is 1 ppb susceptibility/μgFe/g wet tissue (ρ = 1.04 g/ml at 36.5 °C) for wet tissue; the unit for the ferritin solution is 1 ppb susceptibility/μgFe/ml and the corresponding theoretical value is 1.27 ppb/μgFe/ml.
[b] GP: globus pallidus; PUT: putamen; CN: caudate nucleus; RN: red nucleus; SN: substantia nigra; TH: thalamus; DN: dentate nucleus; WM: white matter; GM: gray matter.
[c] SO: single orientation; MO: multiple orientation; TKD: truncated k-space division.
[d] H&S: (Hallgren and Sourander, 1958).

[1] Table replicated from the reference with permission.

Chapter Four

4 Assessing Global and Regional Iron Content in Deep Gray Matter as a Function of Age Using Susceptibility Mapping

As seen in previous chapters, iron content, mostly in the form of ferritin, has been reported to be well-correlated with the aging brain under both normal and diseased conditions. In order to assess the changes of abnormal iron content with more confidence, a robust, sensitive and reliable *in vivo* baseline is required. In this chapter, susceptibility changes of deep gray matter nuclei in a cohort of 174 normal subjects have been investigated using QSM maps as a function of age with the aim of establishing such as baseline.

4.1 Introduction

Iron is the most abundant transition metal in the brain, and plays a key role in a number of brain cellular processes including oxygen transport, electron transfer, neurotransmitter synthesis, myelin production, and mitochondrial function.(Hare et al. 2013; Stankiewicz et al. 2007). However, the useful redox cycling between ferrous (Fe^{2+}) and ferric (Fe^{3+}) iron can also make iron toxic when it is not safely bound in ferritin, because free or poorly liganded Fe(II) can react with H_2O_2 to generate highly reactive hydroxyl ions (Udipi, Ghugre, and Gokhale 2012). Both conditions of iron overload and iron deficiency (Hare et al. 2013) are associated with human brain diseases. Elevated iron is often a feature of neurodegenerative diseases such as multiple sclerosis (MS) (Khalil et al. 2011), Alzheimer's disease (Antharam et al. 2012), Parkinson's disease (Popescu et al. 2009), Huntington's disease (Rosas et al. 2012), ferritinopathies (Baraibar et al. 2008), and subarachnoid hemorrhage (Gomes et al. 2014). Histological in vitro analysis has demonstrated that iron accumulation rates in various

gray matter (GM) structures are different throughout an individual's lifetime (Hallgren and Sourander 1958). To further elucidate the involvement of iron in neurodegenerative disorders, a robust in vivo quantitative noninvasive assessment of normal brain iron deposition over time might be useful. In this study we will attempt to provide such a baseline that can be used to differentiate normal from abnormal iron levels in patients with potential increases in iron content not just globally (the entire structure) but also locally (for the high iron content region).

As pointed out in chapter 3, a variety of MRI methods have been used to quantify brain iron over the years including FDRI (field-dependent relaxation rate increase), R2, R2*, phase, and quantitative susceptibility mapping (QSM) (Langkammer et al. 2010; Bilgic et al. 2012; Haacke, Miao, et al. 2010; Zheng et al. 2013). Most approaches in use today involve either R2 relaxation or susceptibility mapping. Although R2 has a linear correlation with iron concentration (Langkammer et al. 2010), parameters generated from gradient echo sequences (GRE) are more sensitive to the local susceptibility induced magnetic field inhomogeneity caused by the presence of iron (Reichenbach et al. 1997). Magnetic susceptibility differences in brain tissues can come from a variety of sources, such as paramagnetic ferritin iron, blood, diamagnetic myelin content, chemical exchange, and fiber orientation (Langkammer, Krebs, et al. 2012). Since the myelin content is negligible in GM, it is currently assumed that the magnetic susceptibility of GM is dominated by ferritin iron (Hallgren and Sourander 1958). R2* has been shown to be a sensitive MRI parameter to estimate iron content in deep GM (Langkammer et al. 2010). On the other hand, phase images and QSM can both distinguish paramagnetic from diamagnetic materials, whereas R2 and R2* cannot.

Phase has been used to represent iron content in the past (Haacke, Miao, et al. 2010; Haacke et al. 2007). However, phase mapping suffers from nonlocality of the magnetic field distribution, so it does not provide accurate local anatomical information (Deistung et al. 2013). This makes it difficult to consistently and accurately estimate the iron content. In the last few years, QSM has been introduced to overcome the nonlocal effects of phase and to generate the susceptibility maps (Liu et al. 2009; Schweser et al. 2011; Wharton and Bowtell 2010; Haacke, Tang, et al. 2010; Haacke et al. 2015). QSM is a post-processing method that reconstructs source images directly from the phase images (Deville, Bernier, and Delrieux 1979; Tang et al. 2013). Both postmortem experiments (Zheng et al. 2013; Langkammer, Schweser, et al. 2012; Sun et al. 2015) and in vivo (Bilgic et al. 2012; Schweser et al. 2011; Wharton and Bowtell 2010; Shmueli et al. 2009) have demonstrated strong correlations between magnetic susceptibility assessed by QSM and known iron concentrations of different structures in the brain (Hallgren and Sourander 1958). However, the reported correlations were not consistent between the in vivo and in vitro results. Also, these in vivo studies only reported susceptibility measurements of the overall structure, which showed large scattering and hampered the use of the estimated normative values in clinical use and caused a loss of ability to detect subtle local iron deposition changes.

Our goal in this chapter is to produce a quantitative magnetic susceptibility baseline as a function of age for each structure as a whole and on a regional basis to study the presence of abnormally high iron content and to establish an in vivo quantitative conversion factor between magnetic susceptibility and iron concentration.

4.2 Materials and Methods

4.2.1 Subjects

A total of 188 subjects were enrolled and scanned at Dalian First Affiliated Hospital, China with signed informed consent approved by the Institutional Review Board. Collecting data took about 6 months. Exclusion criteria were: history of neurological or psychiatric conditions; head trauma; drug and alcohol abuse; and brain surgery. These participants did not show any focal parenchymal loss, infarction, resection, or large hyperintensities in their brain on T2-weighted images. Seven subjects were excluded because of motion during scans. Another seven subjects were not included due to strong sinus artifact. By excluding those cases, we included 174 normal subjects in this study (age, 45.1 ± 14.2 years; range, 20–69 years; 85 females, 89 males).

4.2.2 MR Parameters

Imaging of the brain was performed using a 1.5T MR scanner (HD, General Electric, Milwaukee, WI) equipped with an eight-channel phased array head coil. The imaging plane was oriented parallel to the anterior–posterior commissural (AC-PC) line. A 3D gradient-echo sequence was applied to acquire images for QSM reconstruction. The imaging parameters included: repeat time/echo time (TR/TE) = 53/40 msec, flip angle = 20º, slice thickness = 3 mm, 40 slices, bandwidth/pixel = 122 Hz/pixel, field-of-view (FOV) = 24 cm, and matrix size ($N_x \times N_y$) = 384 × 320, yielding an in-plane resolution of 0.60 × 0.75 mm. A SENSE (sensitivity encoding) factor of 2 was used. The total scan time was 6 minutes, 28 seconds.

4.2.3 Image Processing and Analysis

QSM images were reconstructed using the MATLAB-based toolbox SMART 2.0 (MRI Institute for Biomedical Research, Detroit, MI). Four steps were applied to generate the resulting QSM images: brain extraction (BET) (Smith 2002), phase unwrapping (3DSRNCP) (Abdul-Rahman et al. 2007), background field removal (SHARP) (Schweser et al. 2011), and an iterative QSM approach (Haacke, Tang, et al. 2010; Tang et al. 2013). The magnitude images were used to extract the brain tissue. Similar to equation (2.43), the original susceptibility maps were derived from the following equation (for a right-handed system) (Haacke, Tang, et al. 2010):

$$\chi(r) = FT^{-1}\left(\frac{1}{\frac{1}{3} - \frac{k_z^2}{k_x^2 + k_y^2 + k_z^2}} . FT\left[\frac{\phi(r)}{-\gamma B_0 T_E}\right]\right) \tag{4.1}$$

where $\phi(r)$ is the phase distribution, T_E is the echo time, B_0 is the main magnetic field strength, γ is the gyromagnetic ratio for hydrogen protons, k_x, k_y, and k_z are coordinates in k-space. The ill-posed nature from the denominator term was overcome by an iterative approach to obtain artifact-free susceptibility maps (Tang et al. 2013). An example resulting QSM image and images from intermediate processing steps are shown in Figure 4.1.

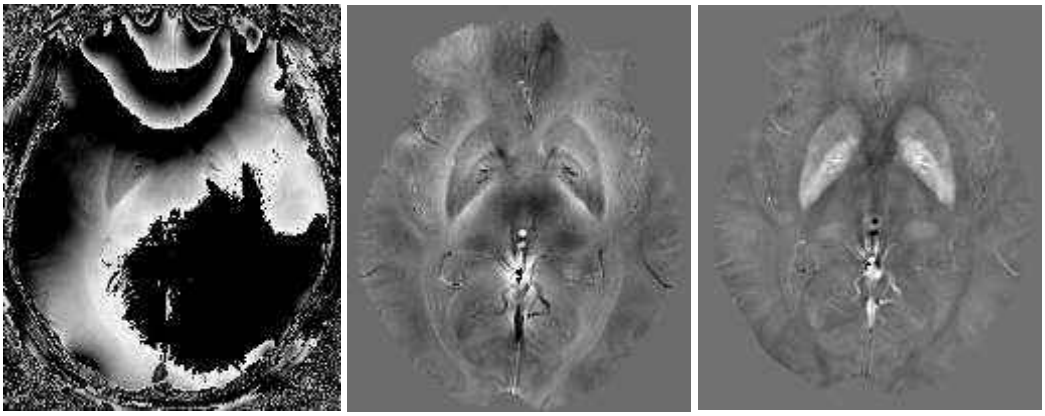

Figure 4.1 Left: Original phase image. Middle: Phase image after performing brain extraction, phase unwrapping, and background field removal. Right: Magnetic susceptibility map (iterative QSM map). The three images are the same slice from the same case. In the susceptibility map, bright signal intensities in the GM nuclei represent high magnetic susceptibility which relates to high iron content.

We quoted the values measured directly from the susceptibility maps to avoid the errors caused by reference selection. If white matter dominates the signal then these will be susceptibility changes relative to white matter.

4.2.4 Whole-Region (Global) Analysis

The susceptibility values in the regions of interest (ROIs) were assessed by segmenting these structures manually based on their anatomical features in the susceptibility maps. To evaluate the magnetic susceptibility of each nucleus in 3D, multiple slices were outlined to cover each entire structure, as shown in Figure 4.2. The 3D ROIs were traced and analyzed using SPIN software (Signal Processing in NMR, MR Innovations, Detroit, MI).

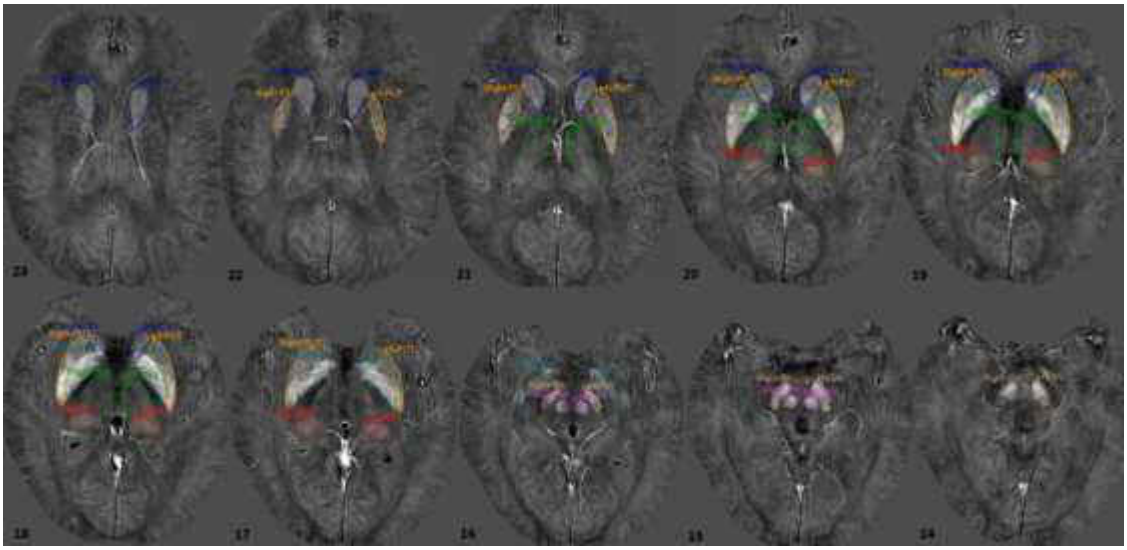

Figure 4.2 Multi-slice 3D ROI's drawn on the QSM maps. Structures include: CN: caudate nucleus (blue), GP: globus pallidus (green blue), PUT: putamen (orange), SN: substantia nigra (yellow orange), RN: red nucleus (violet), PT: pulvinar thalamus (red), and THA: thalamus (green). Numbers on the images are the slice number. Each dataset contains 40 slices.

The GM nuclei assessed on the QSM maps included: caudate nucleus (CN), globus pallidus (GP), putamen (PUT), thalamus (THA), pulvinar thalamus (PT), red nucleus (RN), and substantia nigra (SN). Large blood vessels in the structures were excluded when drawing the ROIs. Bilateral structures were traced on the same slices. The criteria for defining these structures were as follows (number of slices is based on 3mm thick slices):

Caudate Nucleus (CN)

The most superior slice chosen was the one first showing the head of CN. We omitted the thin body part of CN because that part is vascularized, so it is hard to distinguish whether the signal is from veins or iron. Also, with a 3 mm slice thickness the susceptibility value of the thin body of CN may not be reliable. The ROIs of the left and right CN were drawn on 5–6 continuous slices until the structure vanished into the sinus.

Putamen (PUT)

Five to six continuous slices were outlined. For most of the cases, the PUT starts 1 to 2 slices lower than the CN.

Globus Pallidus (GP)

The GP starts from 1–2 slices lower than the PUT and usually presents on 4–5 continuous slices. It ends on the same level or one slice lower than the PUT. The slices with striations were avoided since they contain strong amounts of mineralization likely unrelated to base iron.

Red Nucleus (RN)

The circular shaped RN appears on 2–3 continuous slices.

Substantia Nigra (SN)

The contours of the SN were delineated on 3–5 continuous slices, which included the same slices where the RN was drawn and 1–2 slices below the RN.

Thalamus (THA)

The THA was traced from inferior to superior. It was drawn from either the first or second slice above the SN and usually continued for 4 slices.

Pulvinar Thalamus (PT)

PT starts in the same slice as the THA or one slice below the THA and is visible in 4–5 slices for the most part.

To correlate the magnetic susceptibility with the iron concentration reported by Hallgren and Sourander (Hallgren and Sourander 1958) the scatterplots of non-heme iron versus age in the GP, PUT, and THA were duplicated electronically from a scanned version of Hallgren and Sourander's article by using WebPlotDigitizer v. 2.6 (developed by Ankit Rohatgi). The reason to duplicate their data was to match the subject age range when doing the comparisons.

4.2.5 Two-Region (Regional) Analysis

For each ROI, an age-related threshold was applied to split it into a low iron content region (RI) and a high iron content region (RII). The thresholds used were the upper 95% prediction interval values for the whole-region analysis linear regressions. Any pixels with iron content above this threshold were allocated to RII, the high iron content region. The correlation between age and average susceptibility of RII were analyzed in this chapter as well. This is the first time a two-region analysis technique has been used in a QSM iron study.

4.2.6 Robustness of Global and Regional Analyses

In order to evaluate the robustness of global and regional analyses, three approaches that might affect the results were evaluated. First, the top slice for each structure was excluded and the linear regression parameters (i.e. slope and Pearson correlation coefficient) and hemisphere differences were compared to the values of the original ROIs. Second, the same steps were performed for the exclusion of the bottom slice. Third, we changed the thresholds from 95% prediction interval to 99% interval, which forces an even higher iron content in defining RII. (Tables of RII robustness tests can be found in APPENDIX B)

In addition, by using the first and the second approach we calculated the systematic error for the comparison between the two hemispheres. For each ROI, the changes shown in the first and second approach were averaged and a standard deviation was calculated and equated to the systematic error. The systematic error was combined with the hemisphere standard error by taking the square root of the sum of squares of the standard and systematic errors. This total error was used to test whether the measurement error could affect the hemisphere difference results.

4.2.7 Statistical Analysis

The statistical analysis was performed using Microsoft Excel 2013 and MATLAB R2012a (MathWorks, Natick, MA). $P < 0.05$ was considered significant. The susceptibility differences between left and right hemispheres in different structures of interest were tested by paired t-tests. Pearson correlation analysis was applied to investigate the relation between susceptibility and age in each structure. A Pearson correlation coefficient larger than 0.5 was considered a strong relationship. Linear regression models were used to fit the data. The susceptibility means and standard deviations (SDs) were calculated for each structure.

A whole-region (global) analysis was used to determine the relationship between magnetic susceptibility and iron concentration from the 174 normal controls. Two methods were used in our study. First, the iron concentrations published by Hallgren and Sourander (Hallgren and Sourander 1958) in their scatterplots (GP, PUT, and THA) were grouped into five bins (each decade as a group for subjects from 21–70 years old). The reason why CN, RN, SN, and PT were not included in this test was that Hallgren and Sourander's article did not provide the scatterplots for those nuclei. With those averages from matched age groups, linear regression models were used to test the correlation between the iron concentrations assessed with

postmortem samples and the magnetic susceptibility as determined from our 174 normal controls. Second, the putamen was used as a specific test against the Hallgren and Sourander article because it showed the strongest iron-age dependency. Linear regression was used to find the correlation between susceptibility and the iron concentration.

4.3 Results

In the global analysis, significant differences for the mean susceptibility between the left and right hemispheres were found in all nuclei, at least in one decade, except for the GP. THA and SN, however, showed significant differences in all age intervals. Overall, for each of the five decades, the GP had the highest susceptibility, followed in decreasing iron content by the SN, RN, PUT, CN, PT, and THA.

Table 4.1 shows the detailed statistics of the hemisphere comparisons for the mean susceptibility in RII. From the two-region analysis, we found in the PUT (right > left, except the 20–30 year decade, $P < 0.01$), THA (left > right, $P < 0.001$), and SN (left > right, $P < 0.01$), all five decades showed significant mean susceptibility differences between the left and right hemispheres. For the CN, there was no difference between the two hemispheres for the young subjects ($P > 0.05$) (younger than 40 years), while after the age of 40 years RII susceptibility in the right hemisphere was significantly higher than in the left hemisphere ($P < 0.01$). For the GP, PT, and RN, there was no significant difference between the two hemispheres ($P > 0.05$). These differences remained significant even for the three modified analyses of dropping the upper or lower slice or changing the prediction interval from 95% to 99%. However, by including the systematic error (1.7 ppb by calculation), many structures lost the hemispheric difference significance; only the SN still retained the significance in all the decades. The structures that still showed a significant difference between the left and right hemisphere after combining the systematic error are marked as bold in Table 4.1.

Table 4.1 Statistics Table of the Susceptibility Comparisons between the Left and Right Hemispheres in RII for Difference Intervals.

Decade	Hemisphere/p-value	CN	GP	PUT	THA	PT	RN	SN
20-30 yr (32 cases)	**Left (ppb)**	69.1±5.2	208.8±6.6	76.7±5.6	**32.4±3.4**	69.7±2.3	123.0±9.7	**177.2±12.9**
	Right (ppb)	69.8±4.7	206.2±9.0	77.6±5.9	**27.3±3.3**	68.4±2.7	121.2±4.5	**170.1±16.5**
	p	0.22	0.02	0.09	**<0.001**	0.01	0.09	**<0.001**
31-40 yr (38 cases)	**Left (ppb)**	76.9±6.5	213.3±8.9	96.9±10.5	**36.2±6.4**	75.8±6.5	140.7±13.5	**187.7±15.2**
	Right (ppb)	78.2±5.8	211.5±6.9	100.8±11.3	**31.1±6.5**	74.9±6.6	139.8±12.3	**178.9±13.9**
	p	0.16	0.05	<0.01	**<0.001**	0.17	0.44	**<0.001**
41-50 yr (32 cases)	**Left (ppb)**	86.5±6.9	218.8±9.8	118.1±11.9	37.5±9.1	80.3±9.4	164.4±13.7	**197.5±15.4**
	Right (ppb)	90.8±7.5	219.7±9.9	123.6±13.4	34.1±9.9	80.7±10.2	161.7±15.1	**188.8±15.1**
	p	<0.001	0.33	<0.01	<0.001	0.64	0.2	**<0.001**
51-60 yr (45 cases)	**Left (ppb)**	94.4±8.9	220.5±7.1	**133.8±14.7**	35.7±7.7	81.1±7.3	172.1±15.4	**201.5±14.7**
	Right (ppb)	98.7±9.0	223.8±7.0	**142.3±13.7**	30.4±6.6	79.3±7.4	170.1±15.1	**187.5±15.8**
	p	<0.01	<0.01	**<0.001**	<0.001	<0.01	0.08	**<0.001**
61-70 yr (27 cases)	**Left (ppb)**	101.6±10.8	224.4±8.6	**146.3±16.9**	33.4±6.8	83.2±7.9	181.1±12.9	**201.8±10.1**
	Right (ppb)	105.5±9.5	228.9±8.2	**159.2±18.1**	29.1±9.0	82.5±9.6	177.3±14.2	**195.5±11.2**
	p	0.01	<0.001	**<0.001**	<0.001	0.62	0.17	**<0.01**

Susceptibility values are quoted as mean ± standard deviation for each decade. Left: left hemisphere. Right: right hemisphere: P-value of the paired t-tests. CN: caudate nucleus. GP: globus pallidus. PUT: putamen. SN: substantia nigra. RN: red nucleus. PT: pulvinar thalamus. THA: thalamus. Bold numbers highlight the structures and decades which showed significant differences between the left and right hemispheres, even after taking the systematic error into account.

Figure 4.3 shows the susceptibility changes as a function of age in the right hemisphere GM nuclei from the whole region analysis (the plots for the left hemisphere are shown in APPENDIX A). Linear regression parameters for this region are also shown in Table 4.3. In the PUT, CN, and RN the magnetic susceptibility appears to be linearly correlated with age ($R > 0.5$, $P < 0.05$). The susceptibility distributions across ages are quite scattered in the GP, SN, and PT, with limited age dependency ($R < 0.25$). In the THA, the susceptibility decreases with age ($R = –0.31$, $P < 0.05$). According to the slopes of the whole-region analysis, the susceptibility of the PUT shows the most rapid increase as a function of age with a changing rate of 1.29 ± 0.10 ppb/year, and then followed by the RN (1.24 ± 0.14 ppb/year), CN (0.48 ± 0.06 ppb/ year), SN (0.45 ± 0.14 ppb/year), PT (0.24 ± 0.09 ppb/ year), and GP (0.17 ± 0.10 ppb/year). The THA shows decreased susceptibility with age, with -0.16 ± 0.04 ppb/year. Also, the correlations between brain iron deposition and age reported in our study are consistent with other published studies as shown in Table 4.2

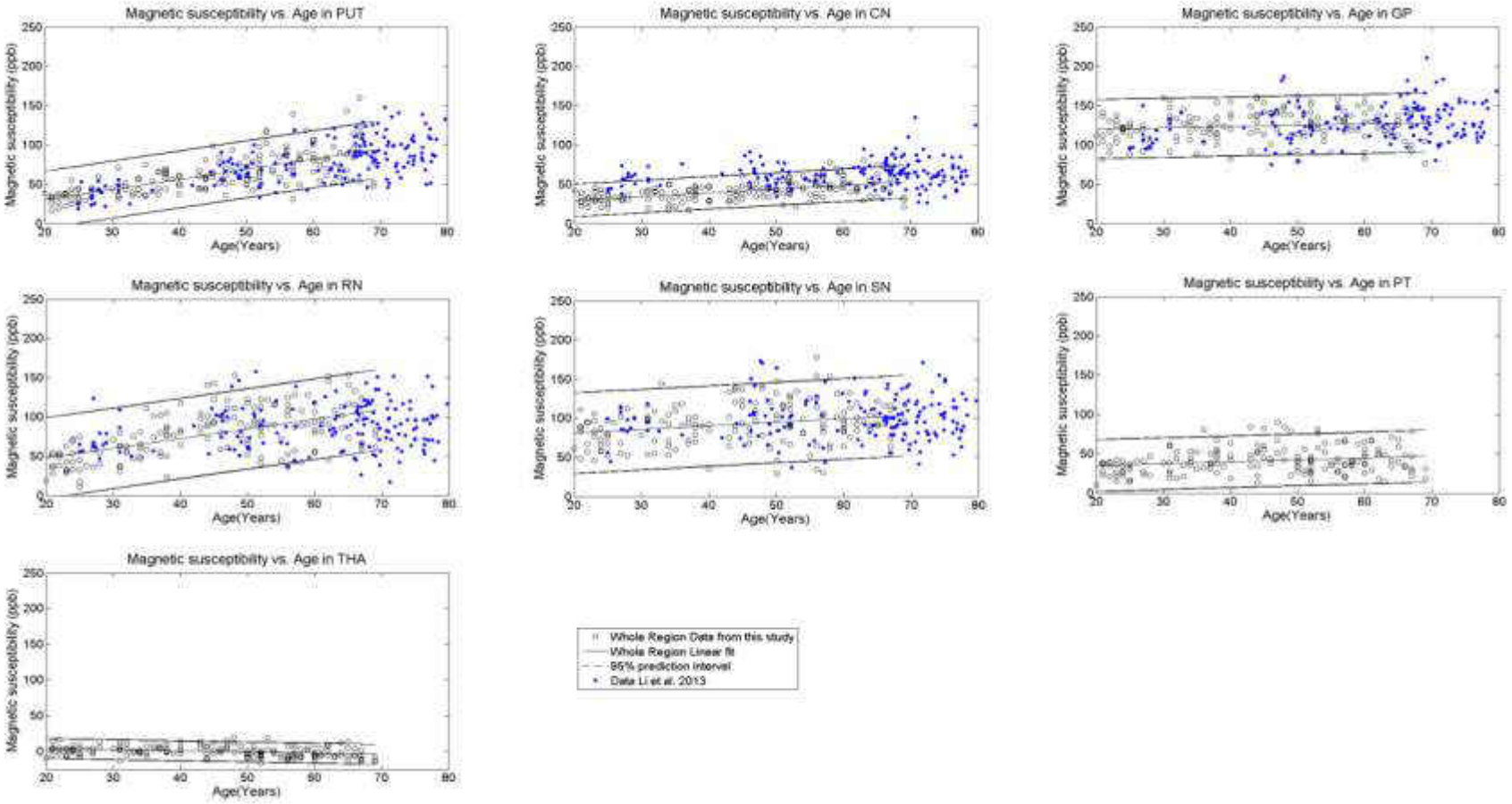

Figure 4.3 Whole-region magnetic susceptibility changes with age in different GM nuclei. The susceptibility values reported in this study are highly consistent with Li *et al.*'s study (Li et al. 2014). Strong positive linear correlations are found in PUT, CN, and RN. Mild positive linear correlations are shown in GP, SN, and PT and weak negative linear correlation in THA. Black circles: current study data. Blue dots: values published by Li *et al*. Black line: linear regression fitting for the current study data.

Table 4.2 Linear Correlations between Iron-Related Parameters (Susceptibility, R2*, Phase) and Age.

Structures	Authors/Method	PCC (R) (20 yr and up)	Field (Tesla)	Subject age range	Sample size
PUT	**Susceptibility**/This study	0.69 (L), 0.71 (R)	1.5	20-69	175
	R2*/Aquino et al. (2009)	Strong*	1.5	1-80	80
	R2*/Cherubini et al. (2009)	Strong**	3	20-70	100
	R2*/Peran et al. (2009)	0.73(L), 0.60(R)	3	20-41	30
	Δ**R2***/Haacke et al. (2010)	0.73(L), 0.72(R)	1.5	20-69	100
	R2*/Li et al. (2013)	Strong*	3	7-83	174
	Phase/Xu et al. (2008)	0.67	1.5	22-78	78
	Phase/Haacke et al. (2010)	0.60(L), 0.59(R)	1.5	20-69	100
	Susceptibility/Li et al. (2013)	0.64	3	20-83	160
	Cadaveric/Hallgren & Sourander (1958)	0.42	N/A	20-70	47
CN	**Susceptibility**/This study	0.50 (L), 0.55 (R)	1.5	20-69	175
	R2*/Aquino et al. (2009)	Weak*	1.5	1-80	80
	R2*/Cherubini et al. (2009)	Strong**	3	20-70	100
	R2*/Peran et al. (2009)	0.47(L), 0.44(R)	3	20-41	30
	Δ**R2***/Haacke et al. (2010)	0.76(L), 0.66(R)	1.5	20-69	100
	R2*/Li et al. (2013)	Strong*	3	7-83	174
	Phase/Haacke et al. (2010)	0.46(L), 0.32(R)	1.5	20-69	100
	Susceptibility/Li et al. (2013)	0.19	3	20-83	160
RN	**Susceptibility**/This study	0.59 (L), 0.57 (R)	1.5	20-69	175
	Δ**R2***/Haacke et al. (2010)	0.72(L), 0.67(R)	1.5	20-69	100
	R2*/Li et al. (2013)	Weak*	3	7-83	174
	Phase/Haacke et al. (2010)	0.55(L), 0.56(R)	1.5	20-69	100
	Susceptibility/Li et al. (2013)	0.17	3	1-83	160
GP	**Susceptibility**/This study	0.07 (L), 0.13 (R)	1.5	20-69	175
	R2*/Aquino et al. (2009)	Good*	1.5	1-80	80
	R2*/Peran et al. (2009)	0.25(L), 0.23(R)	3	20-41	30
	Δ**R2***/Haacke et al. (2010)	0.52(L), 0.51(R)	1.5	20-69	100
	R2*/Li et al. (2013)	Weak*	3	7-83	174
	Phase/Haacke et al. (2010)	0.03(L), 0.03(R)	1.5	20-69	100
	Susceptibility/Li et al. (2013)	0.25	3	20-83	160
	Cadaveric/Hallgren & Sourander (1958)	0.14	N/A	20-70	47

SN	**Susceptibility**/This study	0.28 (L), 0.24 (R)	1.5	20-69	175
	R2*/Aquino et al. (2009)	Weak*	1.5	1-80	80
	Δ**R2***/Haacke et al. (2010)	0.43(L), 0.50(R)	1.5	20-69	100
	R2*/Li et al. (2013)	No*	3	7-83	174
	Phase/Haacke et al. (2010)	0.37(L), 0.37(R)	1.5	20-69	100
	Susceptibility/Li et al. (2013)	0.08	3	20-83	160
PT	**Susceptibility**/This study	0.19 (L), 0.20 (R)	1.5	20-69	175
	Δ**R2***/Haacke et al. (2010)	0.63(L), 0.67(R)	1.5	20-69	100
	Phase/Haacke et al. (2010)	0.47(L), 0.48(R)	1.5	20-69	100
THA	**Susceptibility**/This study	-0.28 (L), -0.30 (R)	1.5	20-69	175
	R2*/Cherubini et al. (2009)	Weak**	3	20-70	100
	R2*/Peran et al. (2009)	0.13(L), 0.15(R)	3	20-41	30
	Δ**R2***/Haacke et al. (2010)	0.58(L), 0.63(R)	1.5	20-69	100
	Phase/Haacke et al. (2010)	0.25(L), 0.27(R)	1.5	20-69	100
	Cadaveric/Hallgren & Sourander (1958)	-0.46	N/A	20-70	42

* Linear correlation was evaluated visually in 20 years-old and higher cases since the studies only provided exponential correlation for a larger age range.

** Studies only provided scatter plots but not the PCC (R).

Figure 4.4 shows a close linear relationship between age and RII average susceptibility for the right hemisphere for all structures (the plots for the left hemisphere are shown in APPENDIX A). The slopes and intercepts of the fitted linear equations for RII analysis are also summarized in Table 4.3. The Pearson correlation coefficients (R) for each relationship are also listed in this table. In most GM nuclei including the GP (except for the THA), very tight, strong correlations were shown between age and magnetic susceptibility.

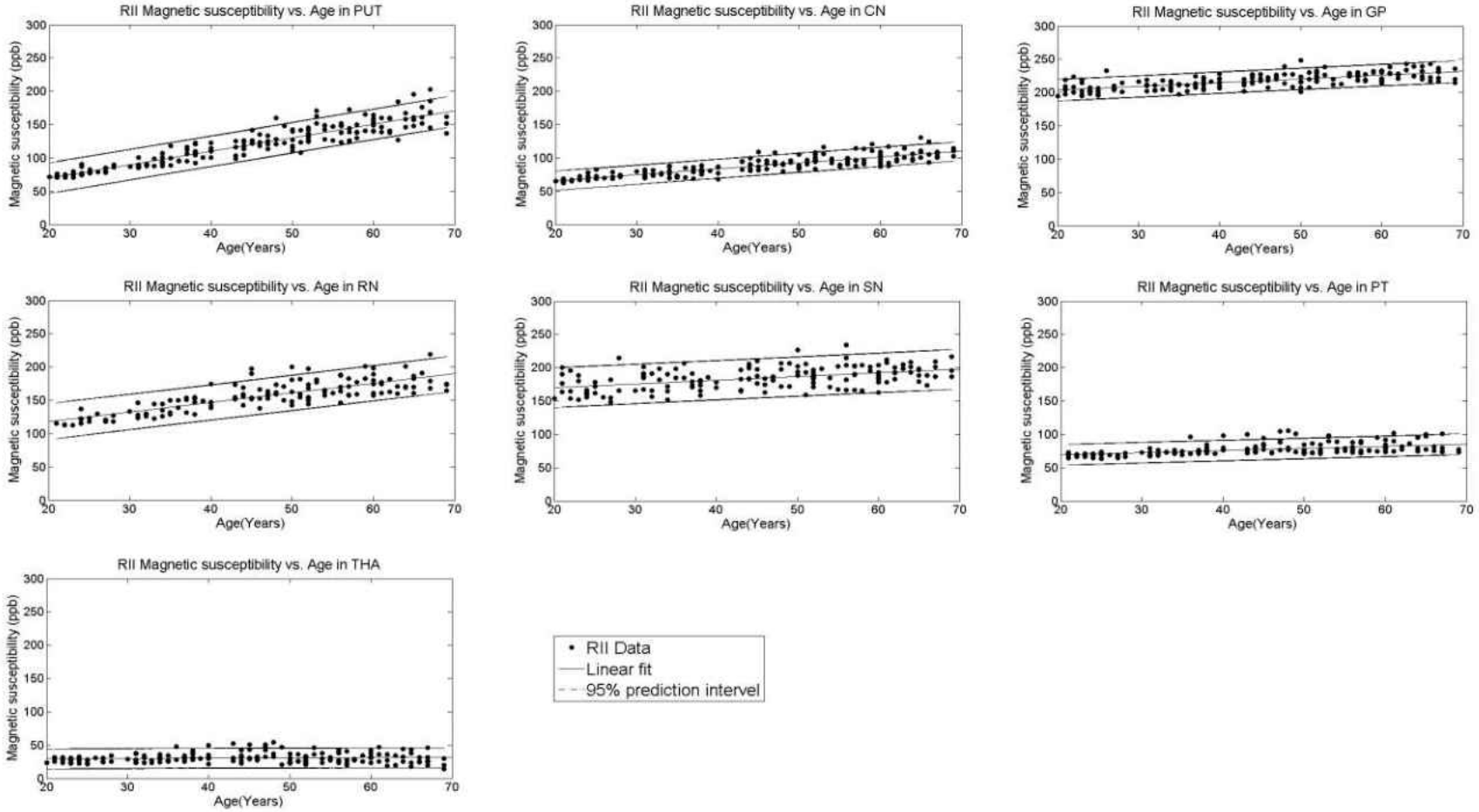

Figure 4.4 RII region magnetic susceptibility changes with age in different GM nuclei for the right hemisphere. Strong positive linear correlations are found in all the structures except THA. Black dots: current study RII data. Black line: linear regression fitting for the current study data.

Table 4.3 Parameters of the Linear Fitting Equations for Susceptibility vs. Age for Both the Whole Region Analysis and Two-Region Analysis.

		$\chi = A \times age + B$					
		Total Region			**High Iron Region**		
		A (ppb/year)	**B (ppb)**	**PCC (R)**	**A (ppb/year)**	**B (ppb)**	**PCC (R)**
CN	Left	0.40±0.05	20.55±2.48	**0.50±0.07**	0.80±0.04	49.47±1.87	**0.84±0.04**
	Right	0.48±0.06	19.59±2.65	**0.55±0.06**	0.89±0.04	48.14±1.83	**0.87±0.04**
GP	Left	0.10±0.10	121.13±4.92	0.07±0.08	0.37±0.04	200.20±2.09	**0.55±0.07**
	Right	0.17±0.10	116.55±4.84	0.13±0.08	0.56±0.04	192.47±2.07	**0.71±0.06**
PUT	Left	1.15±0.09	8.36±4.37	**0.69±0.06**	1.75±0.06	35.57±2.94	**0.91±0.03**
	Right	1.29±0.10	4.14±4.65	**0.71±0.05**	2.02±0.06	29.45±2.93	**0.93±0.03**
SN	Left	0.57±0.15	78.75±7.08	**0.28±0.07**	0.62±0.08	165.13±3.68	**0.54±0.07**
	Right	0.45±0.14	71.95±6.66	**0.24±0.08**	0.56±0.09	158.90±4.04	**0.47±0.07**
RN	Left	1.38±0.14	20.27±6.77	**0.59±0.06**	1.47±0.09	89.88±4.18	**0.83±0.05**
	Right	1.24±0.14	22.57±6.59	**0.57±0.06**	1.44±0.09	89.37±4.31	**0.81±0.05**
PT	Left	0.20±0.08	34.28±3.73	**0.19±0.08**	0.32±0.04	63.46±1.82	**0.54±0.06**
	Right	0.24±0.09	29.99±4.23	**0.20±0.07**	0.32±0.04	62.79±2.07	**0.49±0.07**
THA	Left	-0.14±0.04	12.12±1.76	**-0.28±0.07**	0.03±0.04	3.83±1.82	0.06±0.08
	Right	-0.16±0.04	8.87±1.79	**-0.30±0.07**	0.04±0.04	28.74±1.92	0.07±0.08

Left: left hemisphere. Right: right hemisphere. PCC: Pearson correlation coefficients in bold represent the regression P-value < 0.05.

For the whole-region analysis, when dropping either the upper or lower slice, the highest absolute difference was 0.13 ppb/year for slope and 0.08 for PCC (the relative changes were 27.1% and 30.8%, respectively). However, in the RII analysis, the largest absolute change was 0.07 ppb/year for slope and 0.06 for PCC (the relative changes were 8.75% and 7.23%, respectively). When changing the thresholds from 95% to 99%, the highest absolute change were 0.16 ppb/year for slope and 0.07 for PCC (the relative changes were 11% and 14.9%, respectively). However, we did find that there were small shifts in the mean values (related to missing either the upper or lower slices) whose peak deviation from the original mean ranged from as small as 0.3ppb in large structures to as large as 6.4ppb (3.6ppb) in smaller structures for people over 50 years (less than equal to 50 years).

For the data extracted from the scatter plots in Hallgren & Sourander's paper, after excluding the subjects younger than 20 years old and older than 70 years old, 47 subjects remained with an age of 43.6 ± 14.2 years old. There is no age difference between our normal controls and those 47 subjects. Figure 4.5 shows the correlation between susceptibility measured by MRI *in vivo* and iron concentration from Hallgren and Sourander. The correlation slope was determined by linear regression. Two approaches served to predict iron concentration as explained in section 4.2.7. By using the bin average approach (Figure 4.5 Left), we found $\chi(\mathrm{ppb}) = 0.89\ (\pm 0.03)\mu\mathrm{g/g} * [\mathrm{Fe}] - 48.51\ (\pm 4.09)\mathrm{ppb}$. By using the iron-age equation approach with PUT data (Figure 4.5, right), we found $\chi(\mathrm{ppb}) = 0.93(\pm 0.05)\mu\mathrm{g/g} * [\mathrm{Fe}] - 59.49(\pm 6.43)\mathrm{ppb}$. GP and THA were not suitable for this test because of the lack of strong iron-age relationship after the age of 20 years.

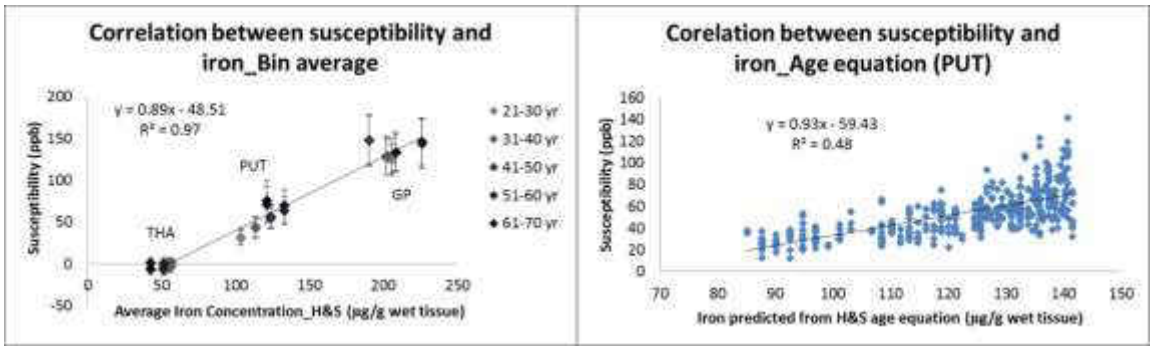

Figure 4.5 Relationship between magnetic susceptibility and iron concentration determined by linear regression. Left: Correlation of the bin average susceptibility with bin average iron concentrations extracted from Hallgren and Sourander's scatterplots (Hallgren and Sourander 1958). The structures included in this plot are GP, PUT, and THA because Hallgren and Sourander only provided the scatterplots of those three structures in their article. Iron–age scatterplots for CN, RN, SN, and PT were not provided in Hallgren and Sourander's article. Right: Correlation of the measured susceptibility with iron concentration calculated from the iron–age equation from Hallgren and Sourander in the PUT. The susceptibility–iron correlations (0.89 ± 0.03 vs. 0.93 ± 0.05 ppb per μg iron/g wet tissue) found with the two methods are consistent.

4.4 Discussion

Left and right hemispheres showed small but significant differences in PUT, THA, and SN. In Xu *et al.*'s study, hemisphere differences were seen in PUT, GP, THA, and SN, but all these four structures showed higher iron content in the left hemisphere (Xu, Wang, and Zhang 2008). However, in our study higher iron was found in the left hemisphere in THA and SN, but PUT showed higher iron content in the right hemisphere. Since iron is co-localized with dopaminergic neurons (Beard 2003), which plays an essential role in regulating voluntary movement, leftward bias of iron content in the SN may correlate with this. However, for the rightward bias of iron in PUT and leftward bias in THA, more data is needed to present conclusive results.

In addition, to test whether the hemisphere differences were due to the way we analyzed the structures, we also calculated the hemisphere differences for the data with a robustness check. Removing either the top or bottom slice led to a systematic error of roughly 1.7 ppb, which if included in the analysis of the difference between left and right hemispheres, for some

structures, would eliminate the significance of a purely white noise estimate of the difference between means in all but those decades where the difference was particularly large.

The major findings in this study are that our results are in agreement with other studies when it comes to global iron analysis as a function of age but add considerable data to the literature and that the high iron content region (RII) can uniquely show iron behavior as a function of age of structures not otherwise available with a global analysis. The correlations are strong in almost all structures other than the THA. Even in the GP, which usually shows no iron content change over the lifespan after the age of 20 years (Hallgren and Sourander 1958; Xu, Wang, and Zhang 2008; Li et al. 2014), we found the Pearson correlation coefficient (R) for age and RII susceptibility to be as high as 0.71 (right side), and the distribution is tight and straight with a slope of 0.56 ppb/year. A previous QSM-iron study (Li et al. 2014) was based on the whole-region analysis, and the individual susceptibility values showed large scatter. Several earlier studies reported better sensitivity to detect abnormal local iron deposition using SWI phase with a two-region analysis (Haacke, Miao, et al. 2010; Habib et al. 2012). However, due to the defects of phase such as nonlocal field effects, phase results are not ideal for acting as baselines for iron content estimation or evolution. Our finding of local iron change in the GM nuclei may provide a means to assess changes in iron content in neurological diseases such as multiple sclerosis and Parkinson's disease and possibly with dementia.

As for the global iron findings, some correlations with age were strong such as for the PUT, CN, and RN, and some were moderate or weak such as for the GP, SN, and PT. The strength of the correlation depended somewhat on the age range used. Changes in the GM nuclei iron as a function of age has been previously investigated with a number of methods such as R2* (Peran et al. 2009; Cherubini et al. 2009; Aquino et al. 2009), phase (Haacke,

Miao, et al. 2010; Xu, Wang, and Zhang 2008), and histopathology (Hallgren and Sourander 1958). Since our data included normal subjects from 20 to 70 years old, we examined the susceptibility by comparing the same age range with other studies. R2* studies by Aquino *et al*. (for PUT, CN, GP, and SN) (Aquino et al. 2009) and Li *et al* (for PUT, CN, GP, SN, and RN) (Li et al. 2014) reported exponential growth in R2* with age, followed by a leveling off, which is consistent with the cadaveric study by Hallgren and Sourander. However, after eliminating the young subjects (younger than 20 years old) in those three studies, all correlations now appear linear. The linear correlation between phase and age is also found in some previous publications (Haacke, Miao, et al. 2010; Xu, Wang, and Zhang 2008). The best linear age dependency is shown in the PUT (Hallgren and Sourander 1958; Haacke, Miao, et al. 2010; Xu, Wang, and Zhang 2008; Peran et al. 2009; Cherubini et al. 2009; Aquino et al. 2009; Li et al. 2014) and sometimes in the CN (Haacke, Miao, et al. 2010; Li et al. 2014; Peran et al. 2009; Cherubini et al. 2009) with R2*/phase/iron growing well into the 80s. This is consistent with our susceptibility trends. Linear regression curves in the GP (Hallgren and Sourander 1958; Haacke, Miao, et al. 2010; Li et al. 2014; Aquino et al. 2009) and SN (Haacke, Miao, et al. 2010; Li et al. 2014; Aquino et al. 2009) are flat for R2*/phase/iron for subjects with ages of 20 years and up; this is also consistent with our findings.

A negative relationship between the susceptibility and age with a small slope was found in the thalamus in this study. This is consistent with what Hallgren and Sourander reported in their postmortem work (Hallgren and Sourander 1958). They claimed a rise in the iron content up to about 35 years old and then a decrease (although they had a limited number of cases between 20 to 30 years). This trend is consistent with Bilgic *et al.*'s finding that the average

susceptibility value in the thalamus was lower in the elderly relative to the young (Bilgic et al. 2012).

Another observation is that the measured susceptibility values are relative to that tissue which dominates the signal and established the main frequency in the MR experiment, in this case the white matter. If the iron content in the white matter goes up with age, then the downward trend we found here for the thalamus would tend to flatten out in reality. This requires further study.

The correlation between magnetic susceptibility and iron concentration found in this study is 0.89 ± 0.03 ppb/μgFe/g wet tissue by the age bin method and 0.93 ± 0.05 ppb/μgFe/g wet tissue by the iron-age function method (Hallgren and Sourander 1958) in the PUT. After applying the algorithm bias correction factor (1.16) (Zheng et al. 2013), the slopes became 1.03 ± 0.03 and 1.08 ± 0.06 ppb/μgFe/g wet tissue, respectively. Those slopes are close to recent studies by Zheng *et al*. (Zheng et al. 2013) and Langkammer *et al.* (Zheng et al. 2013). In their studies, the susceptibility-iron correlation was investigated by ferritin phantoms and cadaveric brains, and the iron concentrations were measured by inductively coupled plasma mass spectrometry (ICPMS) and X-ray fluorescence (XRF). The slopes reported were 1.11 ppb/μgFe/g wet tissue (ferritin, ICPMS), 1.10 ppb/μgFe/g wet tissue (ferritin, XRF), 0.93 ppb/μgFe/g wet tissue (cadaveric, XRF), and 0.96 ppb/μgFe/g wet tissue (cadaveric, ICPMS).

Another consideration in this study to find the susceptibility-iron correlation is by estimating the iron concentration from the age equations provided in Hallgren and Sourander's article (Hallgren and Sourander 1958). The disadvantage of this method is that there is no one-to-one match for each individual because the equation can only represent the mean iron

concentration throughout the lifespan. Because of this we had to choose a structure that showed a strong age dependency. With the large sample size of 174 and strong age-dependent characteristics in PUT, a very strong correlation between the magnetic susceptibility and iron content was seen.

Since the magnetic susceptibility values are relative, they need to be referenced to a particular origin or tissue type. In some articles, the cerebrospinal fluid (CSF) was chosen as the reference region (Yao et al. 2009; Li, Wu, and Liu 2011). However, due to the fact that the CSF shows a large range of susceptibility values (Lim et al. 2013), we used the measured susceptibility directly.

The limitations of this study include a limited age range from 20 to 70 years of age, a thick slice of 3 mm, and possible aliasing. However, by combining Li *et al.*'s recent study (Li et al. 2014), it is clear that there is a continuing linear trend for increasing iron, as predicted by our analysis. The thicker slice of 3 mm could in principle lead to a reduced value of susceptibility because of partial volume effects. Another limitation is the lack of confirmation of iron concentration measurements in individuals by means of histochemical correlation; as a result, an indirect approach to previously reported data was chosen (Hallgren and Sourander 1958).

In conclusion, the results of this study show that a two-region analysis with QSM is a novel, robust and effective way of studying different regions of iron deposition in the deep GM. Almost all structures were seen to have a change in iron using mean iron from the RII analysis. Therefore, these susceptibility-age correlations may serve as a new baseline for determining normal iron content as a function of age in RII that can be used to help determine abnormal iron content levels in a variety of neurodegenerative diseases.

Chapter Five

5 Susceptibility Baseline of the Dentate Nucleus as a Function of Age

In this chapter, a brief background will be given on the dentate nucleus anatomical positioning and physiological functions, followed by its role in abnormal conditions and subsequent MR-related changes. In the end, global and regional quantitative susceptibility baseline as a function of age (the same way they were defined in chapter four) will be established and validated in this structure.

5.1 Introduction

The Dentate Nucleus (DN) is the largest structure, made of nerve cells, which is located in the deep cerebellum and connects it to the brain tissue. The dentate Nucleus got its name because of the toothed-shape edges located bilaterally in the cerebellum.

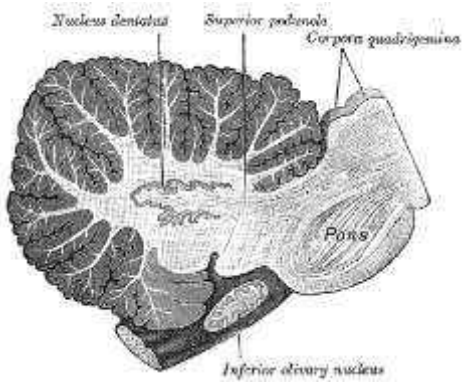

Figure 5.1 Sagittal view of the cerebellum showing the Dentate Nuclei[1]

As one of the vital nuclei in the central nervous system, the Dentate Nucleus has a variety of neurological functions which can basically be divided into two categories (Saab and Willis

[1] Image taken from: Henry Vandyke Carter - Henry Gray (1918) Anatomy of the Human Body.

2003); first, being in charge for those functions which are generally associated with coordination of one or several inputs such as motor tasks, general thoughts and planning. Signals associated with these functions usually travel through the cerebellar cortex before reaching the deep cerebellar nuclei. Second, the output from the cerebellum originates from the deep cerebellar nuclei where it gets processed and sent out to the rest of the nervous system. In addition to being in charge of voluntary movements' control and motor functions, the dentate nucleus also acts as a processor unit in visual and cognitive tasks (Sultan, Hamodeh, and Baizer 2010). The processed signal then gets delivered to other areas of the cortical and non-cortical brain tissue which are responsible for performing these tasks. (Saab and Willis 2003).

The Dentate Nucleus is believed to be involved in a spectrum of normal brain maturation as well as abnormal conditions which can potentially be monitored by MR techniques. More detailed discussions will be given in the following sections of this chapter.

5.2 The Role of the Dentate Nucleus under Abnormal Conditions

Although this deep cerebellar nucleus plays a key role in different processing functions, its deviation from homeostasis might as well be problematic. Over the past decade, there has been great interest in investigating the dentate nucleus in terms of different physiological and pathophysiological interactions under normal and abnormal conditions.

5.2.1 Gadolinium Deposition and Cerebellar Disorders

One of the most recent concerning topics in which this nucleus has been involved is the usage of contrast agents in a variety of diagnostic applications both in pre-clinical and clinical

trials. It is generally believed that the gadolinium ions and the chelating agents used for enhanced diagnostic purposes get discharged through normal renal function. However, to date, by taking advantage of MRI techniques, several recent studies have confirmed noticeable amounts of gadolinium deposition in the human brain, especially in the dentate nucleus and globus pallidus (Kanda, Oba, Toyoda, Kitajima, et al. 2016; Stojanov, Aracki-Trenkic, and Benedeto-Stojanov 2016; Tedeschi et al. 2016; Hu et al. 2016; Ramalho et al. 2016) to the point where the U.S. Food and Drug Administration (FDA) has announced a safety statement asking the radiologists to limit the number of gadolinium-based contrast agents (GBCA) administrations[2].

In 2014, Kanda *et al.* first showed a positive association between the number of previously administered linear GBCAs (e.g. gadopentetate and gadodiamide) and signal hyper-intensity in unenhanced T1-Weighted MR images in the globus pallidus and dentate nucleus due to the presence of gadolinium which supposedly reduces the effective tissue longitudinal relaxation time (Kanda et al. 2014). To date, while the effect of the chelate types with linear molecular structure on the brain gadolinium deposition were also confirmed in other recent research studies both in adult patients (Stojanov, Aracki-Trenkic, and Benedeto-Stojanov 2016; Tedeschi et al. 2016; Kanda, Oba, Toyoda, Kitajima, et al. 2016; Ramalho et al. 2016; Adin et al. 2015) and pediatric patients (Hu et al. 2016; Miller et al. 2015; Roberts and Holden 2016), there is promising evidence that GBCAs carrying macro-cyclic chelating molecules do not tend to accumulate in the brain structures (Kanda, Oba, Toyoda, Kitajima, et al. 2016; Kanda, Oba, Toyoda, and Furui 2016) with an exception of relapsing-remitting multiple sclerosis

[2] http://www.fda.gov/Drugs/DrugSafety/ucm455386.htm

(RRMS) patients. Using T1W images, Stojanov *et al.* has recently shown that cumulative administration of gadobutrol, a macrocyclic GBCA, results in significantly higher T1W signal intensities in RRMS patients within the globus pallidus and dentate nucleus (Stojanov et al. 2016). They have also reported higher rates of unenhanced T1W signal increase, an indication of greater gadolinium accumulation, over shorter period of gadobutrol administration.

From a pathophysiological standpoint, the dentate nucleus is involved in a variety of other diseases as well. Changes in MR parameters could potentially manifest themselves as a biomarker in order to monitor the severity of these disorders as well as their progress. For example, dentate nuclei hyperintensity in Fluid Attenuation Inversion Recovery (FLAIR), T2, and T1-Weighted images are indicative of metronidazole toxicity, L-2-hydroxyglutaric aciduria, and both Fahr's disease and Multiple Sclerosis, respectively, while hypointensities in the dentate nucleus of T2-Weighted images could suggest a case of aceruloplasminaemia (Khadilkar et al. 2016).

5.2.2 Abnormal Iron Deposition in the Dentate Nucleus

The subject of interactions of iron content in the dentate nucleus has been of great interest under either normal or abnormal conditions. As pointed out in previous chapters, an important aspect of iron deposition in the human brain is its correlation with the extent and progression of neurodegenerative diseases. A recent quantitative study done by He *et al.* has confirmed that the susceptibility values in the dentate nucleus of tremor-dominant (TD) Parkinson's disease patients are significantly higher than those of age- and gender-matched healthy adults (He et al. 2016). Since this phenomenon was not seen in Akinetic-Rigidity-dominant (ARD) PD patients, the increased rates of non-heme iron presence in this nucleus can potentially

differentiate between these two PD phenotypes. Also, by taking advantage of iron local paramagnetic contributions to the filtered phase images, Du *et al.* have shown that RRMS patients tend to build up significantly more iron content in deep gray matter nuclei, including the dentate nucleus, compared to the healthy people (Du et al. 2015). Abnormal iron build up has also been reported in right dentate nucleus in Essential Tremor (ET) due to significantly lower T2* values as compared to healthy subjects (Novellino et al. 2013). Furthermore, while non-significant T2, T2' and T2* differences were observed in the dentate nuclei of Friedreich's Ataxia (FRDA) patients in comparison to the normal population[3] in Solbach *et al.*'s work (Solbach et al. 2014), significantly higher T2 values were reported in Bonilha da Silva *et al.*'s study in the dentate nuclei of FRDA patients, suggesting abnormally increased levels of iron content in the cerebellum (Bonilha da Silva et al. 2014).

5.3 Interactions with the Aging Brain

The association between the dentate nuclei iron content and the aging brain has also been investigated in the literature under normal conditions as well as neurological disorders. Regarding neurodegeneration, a recent two-year longitudinal study has revealed a significant increase in the mean phase values of the deep gray matter structures and cerebellar dentate nuclei in RRMS patients between the two time-points, suggesting augmented levels of iron concentration in these regions (Du et al. 2015). On the other hand, under normal circumstances, the consistency between the reported correlations with age is questionable; in 2004, Maschke *et al.* showed a gradual decrease in T1W signal intensity as a function of age which was presumably due to the increased levels of iron content in the elderly (Maschke et

[3] Non-significant transverse relaxation rate difference is basically equivalent to normal levels of iron content.

al. 2004). In contrast with this study, using QSM group comparison, no significant difference between the elderly and the young was detected by Bilgic *et al.* (Bilgic et al. 2012). A more recent work, however, has revealed increasing nonlinear exponential susceptibility-age correlation in the dentate nuclei of healthy subjects across the lifespan in which the positive growth rate almost levels off at higher ages (Li et al. 2014). QSM was also used in Persson *et al.*'s work by which a nonlinear parabolic trend between the magnetic susceptibility (and hence the iron content) of the dentate nucleus and age in healthy adults was reported (Persson et al. 2015). While the previous two studies have shown nonlinear behavior of susceptibility and age in the dentate nucleus, Acosta-Cabronero *et al.* has recently demonstrated a weak and yet significant linear increasing trend of susceptibility as a function of age in this structure (Acosta-Cabronero et al. 2016).

By taking all the aforementioned age-dependent inconsistencies into account as well as the need for a more accurate investigation of diseased conditions in this cerebellar nucleus, a reliable *in vivo* baseline as a function of age is still missing. In order to achieve this goal, the global and regional (i.e. high iron content region) analyses of susceptibility-age correlation will be discussed in the following section.

5.4 Global and Regional Iron-Age Correlations

In order to establish an *in vivo* susceptibility baseline of the dentate nucleus as a function of age, a total of 81 healthy subjects (age: 39.14±12.5, range: 20-61 years old) were recruited for a 3D gradient echo (GRE) sequence using SIEMENS 3.0 T MR scanner with the imaging parameters of: TR = 29 ms, TE = 20 ms, Flip Angle (FA) = 15º, slice thickness = 2 mm, pixel bandwidth = 120 Hz/pxl, matrix size ($N_x \times N_y$) = 448 × 336, and in-plane resolution = 0.51 ×

0.51 mm. The QSM maps were reconstructed using SMART v2.0 MATLAB-based toolbox (MRI Institute for Biomedical Research, Detroit, MI). Brain extraction, phase unwrapping, background field removal and inverse filtering QSM approach were all similar to section 4.2.3 (i.e. BET, 3D-SRNCP, SHARP and iterative QSM, respectively).

5.4.1 Global Analysis

Figure 5.2 shows how 3D regions of interest in the dentate nuclei were manually traced on 4-5 continuous slices of the cerebellar region on QSM maps. The ROIs were drawn using SPIN software (Signal Processing in NMR, MR Innovations, Detroit, MI).

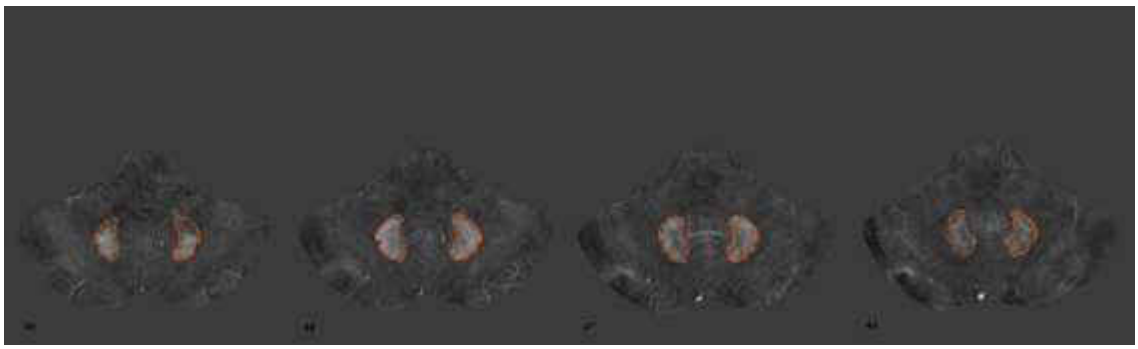

Figure 5.2 3D ROIs of the dentate nuclei within the cerebellum of a 50-year-old healthy volunteer. Slice numbers are shown on the images.

Similar to the whole-region analysis discussed in chapter four, the mean susceptibility value of the whole 3D structure was extracted and plotted as a function of age for each subject. As demonstrated in Figure 5.3, in order to assess the validity of the method, the results from this approach were compared to susceptibility values of the dentate nucleus published in Li *et al*'s work (Li et al. 2014) with the same approximate age range.

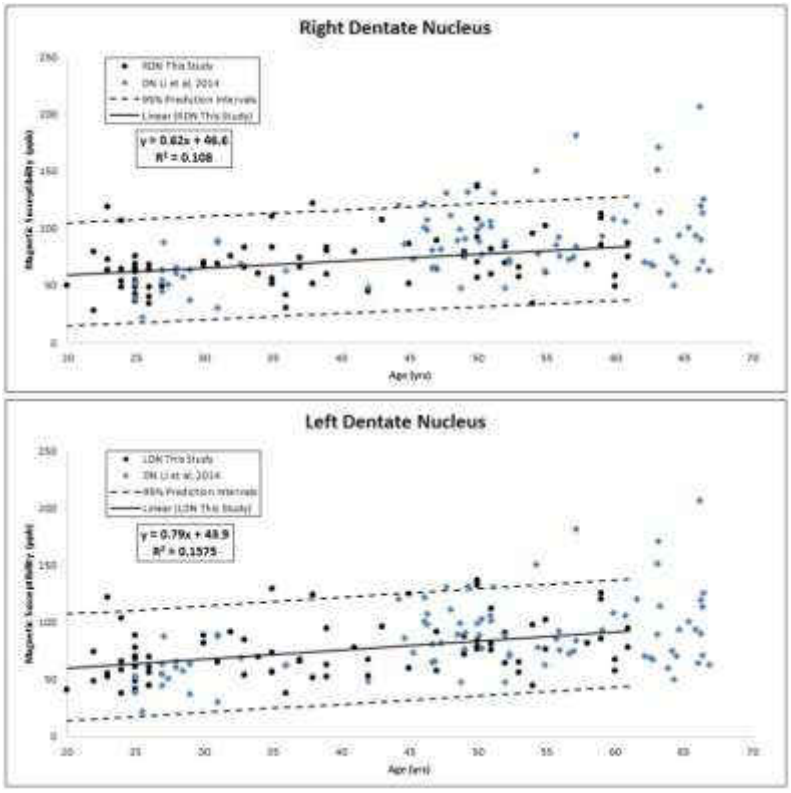

Figure 5.3 Global (whole-region) analysis of magnetic susceptibility changes as a function of age in right and left dentate nuclei as compared to the values reported in Li *et al.*'s study (Li et al. 2014). Within the age range shown above, the results are strongly consistent with each other. Black filled circles: data from the current study. Blue diamonds: results published by Li *et al.* Equations: linear regression line for the fitted data (Solid black). Dashed lines: 95% prediction intervals calculated from the current study.

As demonstrated above, the whole-region analysis of the dentate nucleus is highly in agreement with previously published literature whose results seem to be falling within the same 95% prediction intervals. The general increasing trend of the susceptibility against age, which is also reasonably followed by the results from another study, has been modeled with a linear regression fitting whose parameters are shown in Table 5.1. However, the linear regression equations appear to show higher slope and R-squared values on the left hemisphere as compared to the right one, which with respect to their comparable intercepts brings up the possibility of having a dominant side in terms of iron accumulation (see Table 5.2).

5.4.2 Regional Analysis

The regional high iron content analysis of the dentate nucleus follows the same algorithm as what was described in chapter four. In other words, for either side, the upper bound of the 95% prediction intervals in the global analysis was chosen to define the voxel-wise high iron content region. The age-dependent threshold equations used in the regional analysis were $THR = 0.62*age + 91.7$ for the right DN and $THR = 0.80*age + 90.6$ for the left DN, meaning that at a given age, any voxel value (i.e. magnetic susceptibility) higher than the corresponding calculated threshold would be characterized as a high iron content voxel (RII). Accordingly, any voxel value lower than that threshold would be a part of the low iron content region (RI) such that the sum of the number of voxels in these two regions would be the same as that of the total region. Similar to the global analysis, the mean value of the susceptibility values present in the high iron content region was calculated for each subject and plotted as a function of age (see Figure 5.4 below).

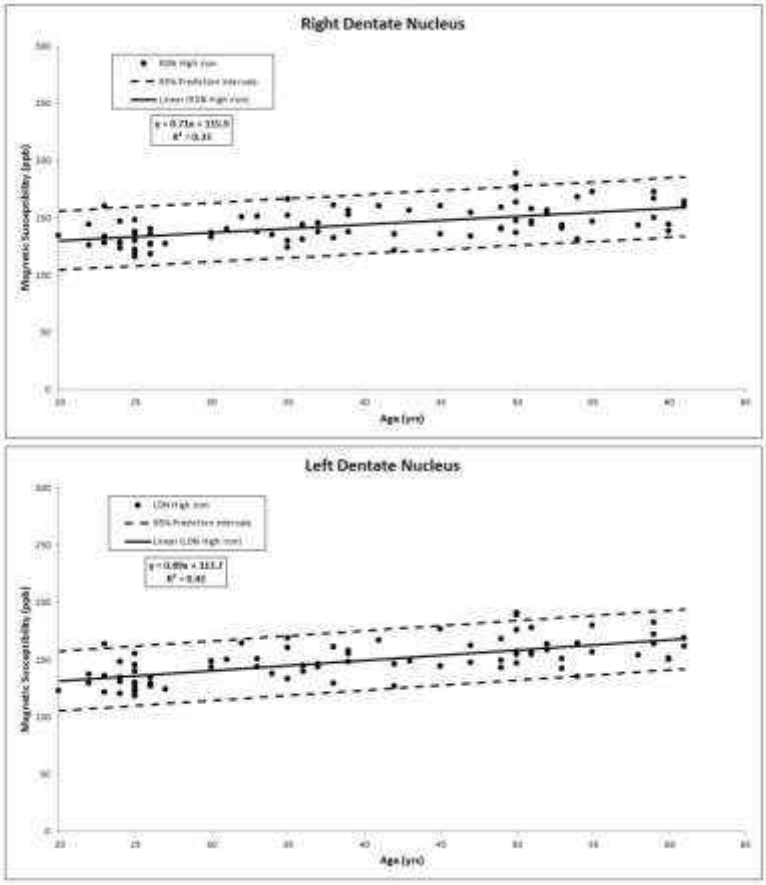

Figure 5.4 Regional (high iron content region) analysis of magnetic susceptibility changes as a function of age in right and left dentate nuclei. Black circles: data from this study. Equations: linear regression lines for the fitted data (Solid black). Dashed lines: 95% prediction intervals.

The linear regression parameters for both global and regional analyses along with their statistical significance tests are also shown in Table 5.1.

Table 5.1 Parameters of the Dentate Nucleus Linear Fitting Equations in both Global and Regional Analyses.

$\chi = A \times age + B$						
	Total Region			**High Iron Region**		
	A	**B**	**PCC**	**A**	**B**	**PCC**
	(ppb/year)	**(ppb)**	**(R)**	**(ppb/year)**	**(ppb)**	**(R)**
Left DN	0.79±0.21	43.90±8.49	**0.40±0.10**	0.89±0.12	113.70±4.74	**0.66±0.08**
Right DN	0.62±0.20	46.63±8.20	**0.33±0.11**	0.71±0.11	115.92±4.67	**0.58±0.09**

PCC: Pearson correlation coefficients in bold represent the regression P-value < 0.05.

As seen above, similar to other basal ganglia and midbrain structures discussed in chapter four, the dentate nucleus also shows stronger linear correlation between magnetic susceptibility and age in the local high iron content region compared to the total structure. That is, having steeper slopes in the linear regression analysis of RII region shows better sensitivity of susceptibility change to age and having higher PCC values confirms enhanced precision of the regional analysis as compared to the global analysis.

5.4.3 Hemispherical Susceptibility Difference

On the other hand, since the slopes of linear regression fitting in both methods are higher in the left hemisphere and given that the intercepts are close to each other, there is a chance that the left hemisphere tends to accumulate more iron content compared to the right side. Table 5.2 shows the hemisphere difference of these two analyses in each decade.

Table 5.2 Dentate Nucleus Hemispherical Susceptibility Comparison in Difference Decades.

Decade	Hemisphere/p-value	Total Region	High Iron Region
20-30 yr (27 cases)	Left (ppb)	60.8±20.2	132.2±10.2
	Right (ppb)	63.0±20.6	134.0±11.5
	p	0.256	0.121
31-40 yr (18 cases)	Left (ppb)	70.0±22.4	**143.7±11.6**
	Right (ppb)	71.9±24.6	**148.4±11.4**
	p	0.473	**<0.01**
41-50 yr (17 cases)	Left (ppb)	82.3±27.8	**152.3±18.1**
	Right (ppb)	88.5±72.8	**158.7±17.3**
	p	0.105	**<0.01**
51-61 yr (19 cases)	Left (ppb)	**75.5±20.6**	**152.8±12.1**
	Right (ppb)	**82.8±21.9**	**160.3±12.5**
	p	**<0.01**	**<0.001**

Susceptibility values are quoted as mean ± SD for each decade. Left: left DN. Right: DN. P-values of the two-tailed paired samples t-tests are quoted. Bold numbers highlight the decades in which there is a significant difference between the hemispheres (p-value<0.05).

The table above represents that only the last decade showed significant susceptibility difference between the two hemispheres in the total region, while regional analysis has revealed significantly higher susceptibility in the left dentate nucleus after the third decade, suggesting the tendency of normal iron deposition on the left side in the high iron content region. However, a more generic statistical analysis shows that by treating the dataset as a whole and not separate decades, the left dentate nucleus demonstrates significantly higher mean susceptibility in both global *(p-value <0.01)* and regional (*p-value < 0.001)* analyses.

All in all, by taking all the discussions in this chapter into consideration, we can conclude that in addition to the global analysis being in agreement with previous literature, the high iron content region shows a more sensitive and less scattered increasing linear measure of changing iron as a function of age in the dentate nucleus. This new susceptibility-age baseline may prove useful for better studying high levels of paramagnetic-component deposition in the dentate nucleus under abnormal conditions, such as gadolinium-based contrast agent (GBCA) build up and neurodegeneration.

Chapter Six

6 Conclusions and Future Directions

6.1 Summary and Conclusions

In this thesis, we used two sets of data to establish an age-dependent baseline for the most important metal present in the human brain, iron, by taking advantage of QSM sensitivity to iron content. In chapter four, the first group of 174 healthy controls was used to construct such a baseline in basal ganglia and midbrain nuclei including seven structures: Caudate Nucleus (CN), Globus Pallidus (GP), Putamen (PUT), Thalamus (THA), Pulvinar Thalamus (PT), Red Nucleus (RN), and Substantia Nigra (SN). The mean values extracted from the whole-structural 3D regions of all these nuclei (also known as global analysis) were in agreement with a similar study (Li et al. 2014) which validates the way these cases were processed. The structure with the highest levels of iron deposition was the Globus Pallidus, as expected, and then followed by the Substantia Nigra, Red Nucleus, Putamen, Caudate Nucleus, Pulvinar Thalamus and Thalamus. In the adult age range used in this group, all the structures showed positive linear trend of global susceptibility change as a function of age, except for the thalamus which showed a negative correlation.

In addition to the global analysis, we have introduced a new concept of monitoring high iron content in these deep gray matter nuclei, known as two-region (RII) analysis whose underlying definition relies on pixel-wise susceptibility values being higher than the upper 95% prediction interval from the global analysis. Extracting the mean susceptibility values from this high iron content region resulted in a more sensitive (i.e. with slopes almost double those in the global analysis), more precise (i.e. less scattered and much tighter trend) and more

robust linear susceptibility-age correlation in almost all structures, as compared to the global analysis. In RII region, the structures with the fastest changing iron as a function of age are in order: putamen, red nucleus and caudate nucleus. These results are in agreement with previous literature and with what is seen in the global analysis.

At the end of chapter four, the correlation between the actual iron concentration (Hallgren and Sourander 1958) and in vivo susceptibility measurements was shown to be 1.03±0.03 ppb/μFe/gTissue by using age bin approach and 1.08±0.03 ppb/μFe/gTissue by using iron prediction equation. This is an almost one-to-one relationship between these two parameters which can help these baselines make better sense.

In chapter five, similar enhancements were seen in the cerebellar dentate nuclei using another set of 81 healthy subjects from a different site. As expected, regional analysis showed higher slopes and R values in the linear regression model. Also, except for the first decade, unlike the global analysis, RII region revealed the dominance of the left hemisphere in terms of high iron accumulation.

In summary, in addition to the global analysis being consistent with previous literature, the two-region approach shown in this thesis was seen to be a more reliable, sensitive iron-age baseline that may prove useful for studying normal and abnormal interactions of iron in the human brain.

6.2 Future Directions

With regard to the contents discussed in this thesis, the following potential future directions are anticipated:

6.2.1 Volumetric Measurements of Iron Content

The measurements reported in this thesis were extracted from the mean values of the 3D ROIs in both global and regional analyses. Since the manually drawn ROIs cover the whole area occupied by each structure, other age-dependent statistical parameters, other than the mean value, can also be extracted from the results including but not limited to: total volume, normalized regional volume, and the total iron concentration (i.e. *mean* × *volume*). These three parameters may add additional information to the results revealed by the mean susceptibility values in either analysis.

6.2.2 Evaluation of Abnormal Iron Content

As discussed in different chapters of this thesis, both iron overload and deficiency can occur in human brain neurological disorders. Neurodegenerative diseases such as Multiple Sclerosis (MS), Parkinson's disease (PD), and Alzheimer's disease (AD) are believed to be characterized by abnormally elevated levels of iron deposition in deep gray matter nuclei. With the new high iron content age-dependent baseline introduced in this thesis, areas of very high iron content existed in each structure will not get neglected (as they tend to be washed out in the global analysis). Thanks to its substantially greater sensitivity and precision, abnormal levels of iron content associated with neurodegeneration could be differentiated from the normal iron-age baseline more efficiently. Same conclusion also applies to evaluating high susceptibility values due to gadolinium deposition in the dentate nuclei of patients undergoing multiple administrations of contrast agents.

6.2.3 Spatial Growth Pattern of Iron Accumulation across the Lifespan

Over the lifespan, in addition to being temporally variable, iron deposition in the human brain is believed to be spatially changing as a function of age as well (Acosta-Cabronero et al. 2016; Aquino et al. 2009). For example, by using R2* maps, Aquino *et al.* showed that in lenticular nucleus, iron deposition tends to occur initiating from posterior towards anterior parts and from medial towards lateral portion as a function of age. Also, Acosta-Cabronero *et al.* used MNI-standardized statistical QSM maps to show cluster-enhanced linearity of spatial susceptibility change across the adult lifespan. Such statistical techniques can also be used in assessing high iron content spatial growth pattern in the human brain, especially in the basal ganglia, midbrain, and cerebellar nuclei.

APPENDIX A

Susceptibility-age correlation of the whole-regional analysis in the left hemisphere is shown in the figure below. Linear regression equations are shown on the plots.

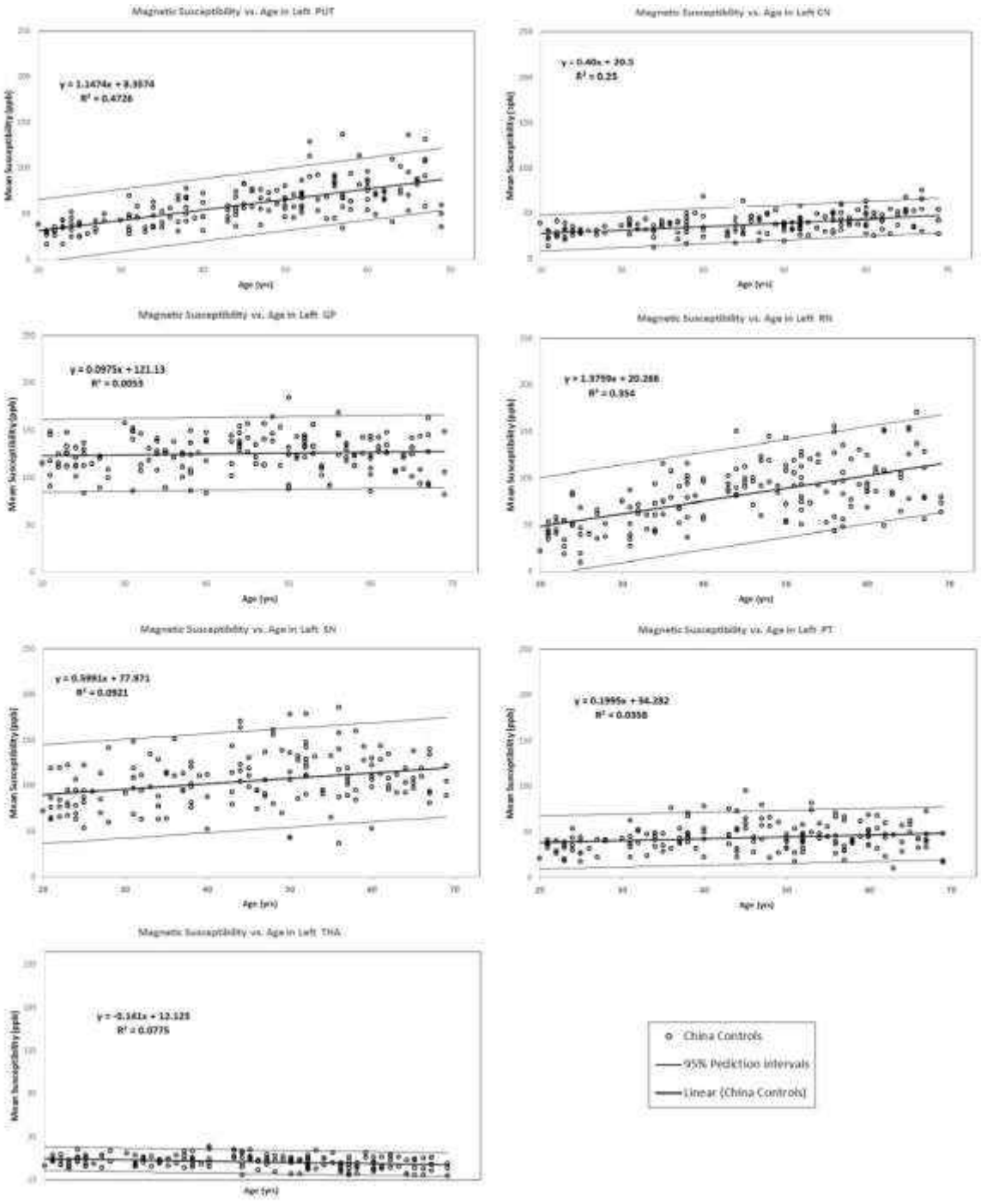

Also, RII region magnetic susceptibility changes with age in different GM nuclei for the left hemisphere are represented in the figure below.

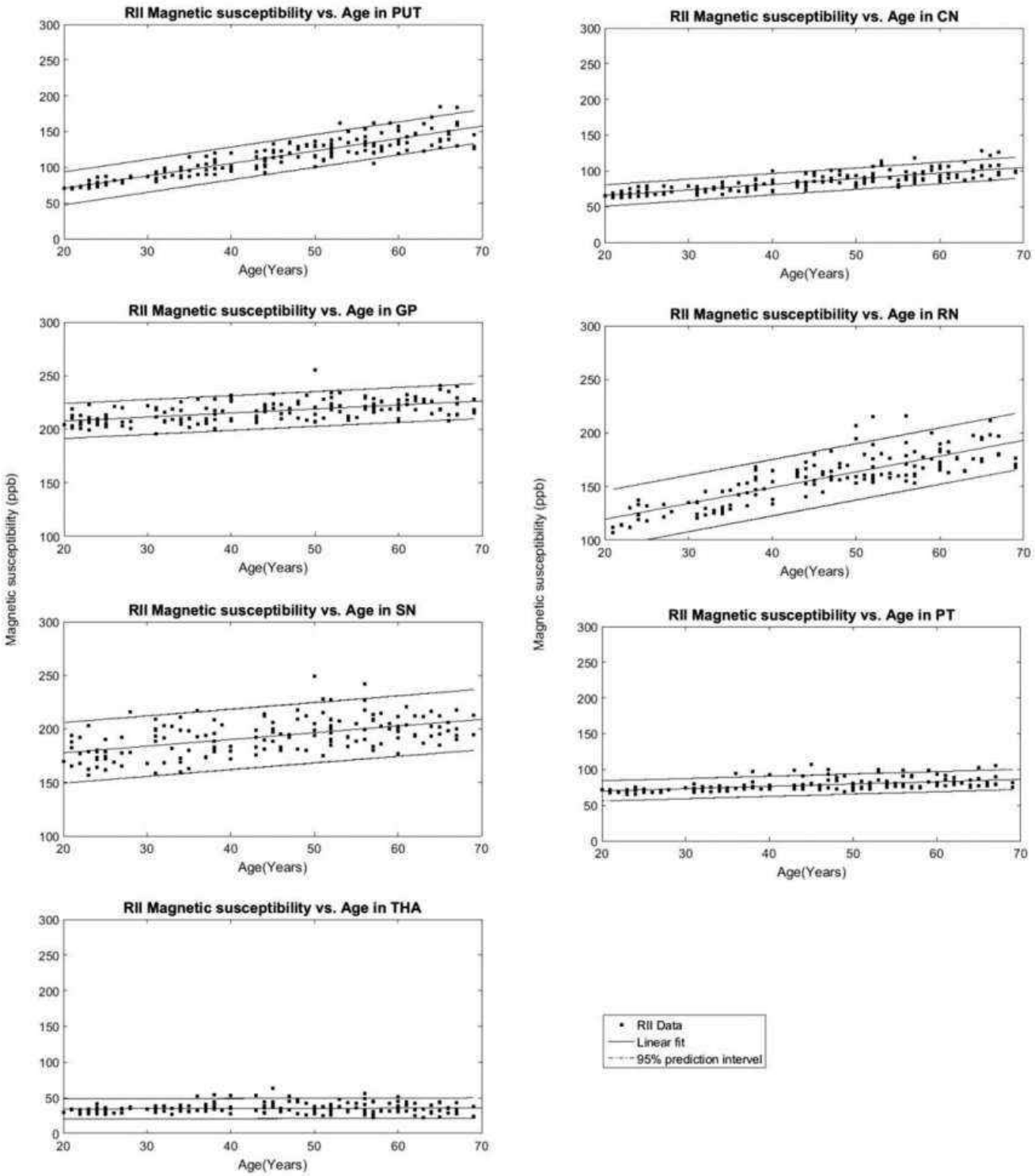

APPENDIX B

The following first three tables were used to test the robustness of RII analysis against systematic error and also using a different method to define the high iron content region.[1] The first two tables describe the changes in hemispherical difference of different decades due to exclusion of one slice from the top and bottom section of all structures, respectively. The third table shows similar changes as a result of using 99% prediction intervals of the global analysis, instead of 95% prediction intervals, to define RII region.

The last table shows hemispherical differences of the regional analysis in all seven structures separated by gender groups for each decade.

[1] The logic behind these tables is the same as what was used in Table 4.1.

Table 0.1 Statistics table of hemispherical RII susceptibility differences after excluding the top slice from each structure.

Decade	Left/Right (ppb)	CN	GP	PUT	THA	PT	RN	SN
20-30 (32 cases)	**Left**	71.0±5.9	**208.9±6.8**	76.8±5.7	**32.9±3.6**	**69.7±2.4**	124.7±9.3	**178.4±13.0**
	Right	71.0±5.2	**206.3±9.0**	77.7±6.0	**28.0±3.8**	**68.5±2.8**	121.5±7.5	**170.2±16.4**
	p	0.96	**0.02**	0.11	**<0.001**	**0.03**	0.09	**<0.001**
31-40 (38 cases)	**Left**	79.1±7.7	213.3±8.8	**97.3±10.8**	**37.0±7.2**	76.2±7.0	141.5±14.2	**190.9±13.0**
	Right	80.1±6.8	211.5±6.8	**101.1±11.5**	**32.3±7.2**	75.0±7.0	141.4±13.5	**180.1±13.5**
	p	0.31	0.05	**0.002**	**<0.001**	0.11	0.95	**<0.001**
41-50 (32 cases)	**Left**	**89.7±8.4**	218.8±10.1	**118.9±12.4**	**39.2±10.4**	80.9±9.9	166.0±15.0	**198.2±16.6**
	Right	**94.5±9.6**	220.0±10.1	**124.2±14.2**	**36.0±11.3**	81.0±11.2	162.1±15.2	**189.4±15.8**
	p	**0.001**	0.19	**<0.01**	**<0.001**	0.98	0.06	**<0.001**
51-60 (45 cases)	**Left**	**97.3±9.8**	**220.7±7.2**	**134.8±15.6**	**36.9±8.2**	**81.0±7.1**	174.7±16.0	**202.0±14.9**
	Right	**101.2±9.8**	**224.0±7.2**	**143.0±14.5**	**32.0±7.2**	**79.6±7.6**	171.6±15.6	**187.9±15.9**
	p	**0.002**	**0.002**	**<0.001**	**<0.001**	**0.04**	0.1	**<0.001**
61-70 (27 cases)	**Left**	105.9±12.4	**224.5±8.7**	**147.3±17.8**	**34.4±7.8**	83.5±8.5	179.8±12.8	**203.2±10.6**
	Right	108.9±10.3	**229.2±8.6**	**160.1±19.2**	**30.5±10.1**	82.7±9.5	176.7±14.1	**196.3±11.7**
	p	0.09	**<0.001**	**<0.001**	**<0.001**	0.57	0.2	**<0.01**

Bold numbers show significant difference between the two hemispheres. *($p<0.05$)*

Table 0.2 Statistics table of hemispherical RII susceptibility differences after excluding the bottom slice from each structure.

Decade	Left/Right (ppb)	CN	GP	PUT	THA	PT	RN	SN
20-30 (32 cases)	**Left**	68.1±6.9	**209.7±7.8**	78.0±10.2	**31.4±3.1**	69.1±3.3	128.0±21	**179.5±15.3**
	Right	68.9±6.3	**207.0±10.0**	79.4±13.4	**26.1±2.9**	68.0±2.8	126.1±17.6	**171.4±18.0**
	p	0.07	**0.02**	0.1	**<0.001**	0.11	0.45	**<0.001**
31-40 (38 cases)	**Left**	**74.4±6.8**	213.0±9.1	**96.6±10.3**	**34.9±5.7**	74.4±6.9	143.3±13.2	**191.0±13.6**
	Right	**77.1±5.0**	211.4±7.5	**99.6±10.3**	**29.2±5.7**	73.3±5.5	141.7±12.6	**180.7±13.8**
	p	**0.01**	0.1	**<0.01**	**<0.001**	0.2	0.52	**<0.001**
41-50 (32 cases)	**Left**	**83.0±6.2**	218.5±10.5	**117.7±11.7**	**35.7±8.0**	79.5±9.2	163.8±14.5	**198.5±15.8**
	Right	**87.2±7.4**	219.4±10.4	**122.4±13.6**	**32.0±8.9**	79.9±10.0	162.5±17.0	**189.2±15.4**
	p	**0.002**	0.33	**0.01**	**<0.001**	0.69	0.54	**<0.001**
51-60 (45 cases)	**Left**	**89.8±7.9**	**220.2±7.2**	**132.8±13.8**	**34.6±7.5**	**79.9±7.0**	174.8±16.9	**202.6±16.0**
	Right	**95.6±7.6**	**223.9±7.0**	**140.7±13.5**	**28.7±6.5**	**78.5±7.2**	171.6±15.7	**188.0±16.9**
	p	**<0.001**	**<0.001**	**<0.001**	**<0.001**	**0.01**	0.11	**<0.001**
61-70 (27 cases)	**Left**	**98.0±11.6**	**224.0±8.5**	**145.4±17.0**	**32.6±6.2**	82.2±7.5	185.4±16.9	**202.6±11.0**
	Right	**103.0±10.6**	**228.7±8.7**	**157.8±18.4**	**27.6±8.5**	81.5±8.7	183.7±16.9	**195.9±11.8**
	p	**<0.001**	**0.002**	**<0.001**	**<0.001**	0.63	0.061	**<0.01**

Bold numbers show significant difference between the two hemispheres. *($p<0.05$)*

Table 0.3 Statistics table of hemispherical RII susceptibility differences after applying 99% prediction intervals instead of 95%.

Decade	Left/Right (ppb)	CN	GP	PUT	THA	PT	RN	SN
20-30 (32 cases)	**Left**	80.5±7.0	229.5±7.5	**89.7±5.8**	**36.7±3.2**	81.7±3.0	151.7±8.6	**197.9±14.0**
	Right	81.1±6.2	228.0±9.4	**91.9±5.9**	**31.7±3.2**	81.1±4.0	146.7±9.3	**191.4±15.0**
	p	0.44	0.2	**<0.01**	**<0.001**	0.35	0.28	**0.001**
31-40 (38 cases)	**Left**	88.8±7.2	234.2±8.3	**110.2±11.1**	**40.8±6.8**	87.2±6.4	163.1±11.2	**211.5±12.8**
	Right	90.5±7.5	233.1±7.5	**115.7±11.3**	**35.7±6.6**	87.3±6.4	162.3±11.5	**201.0±11.7**
	p	0.12	0.19	**<0.001**	**<0.001**	0.97	0.61	**<0.001**
41-50 (32 cases)	**Left**	**98.6±7.8**	**239.8±9.0**	**130.4±11.5**	**42.0±9.4**	92.5±8.6	182.9±13.3	**217.6±17.8**
	Right	**103.8±9.3**	**242.0±8.2**	**137.6±12.6**	**38.7±10.3**	92.1±9.1	181.2±12.4	**208.6±14.4**
	p	**<0.001**	**0.01**	**<0.001**	**<0.001**	0.78	0.34	**<0.001**
51-60 (45 cases)	**Left**	**105.7±9.3**	**241.7±7.1**	**145.4±13.4**	**40.3±7.8**	92.9±7.1	191.2±13.5	**223.9±13.2**
	Right	**110.3±9.5**	**246.6±7.6**	**154.7±12.4**	**35.0±6.9**	91.9±7.7	188.3±11.8	**212.6±12.6**
	p	**<0.001**	**<0.001**	**<0.001**	**<0.001**	0.29	0.09	**<0.001**
61-70 (27 cases)	**Left**	**113.7±11.3**	**246.4±9.0**	**157.8±16.1**	**38.1±6.9**	95.3±6.9	199.0±13.1	**221.3±12.9**
	Right	**117.7±10.1**	**251.4±8.2**	**171.2±17.2**	**34.1±9.1**	95.3±9.8	198.7±11.6	**215.5±11.3**
	p	**0.03**	**0.001**	**<0.001**	**<0.001**	0.99	0.89	**0.04**

Bold numbers show significant difference between the two hemispheres. *($p<0.05$)*

Table 0.4 Statistics table of hemispherical RII susceptibility differences in each decade separated by gender.

Decade	Gender (#Cases)	Hemisphere (ppb)	CN	GP	PUT	THA	PT	RN	SN
20-30 yr	F(14)	**Left**	**66.8±4.2**	209.5±7.1	**75±5.8**	**33.8±3.7**	70±2.2	122.1±10.7	**182±9.6**
		Right	**68.7±3.8**	207.1±9.1	**77±7.2**	**27.1±2.8**	68±2.7	120.6±8.4	**172.8±17.3**
		p	**0.019**	0.153	**0.047**	**<0.001**	0.075	0.436	**0.014**
	M(18)	**Left**	70.8±5.3	208.2±6.3	78±5.3	**31.4±2.9**	69.4±2.5	123.9±9.3	**173.8±14.1**
		Right	70.6±5.3	205.4±9.1	78.1±4.8	**27.5±3.7**	68.7±2.7	121.7±7.2	**168.1±16.1**
		p	0.8	0.058	0.811	**<0.001**	0.077	0.125	**<0.001**
31-40 yr	F(16)	**Left**	76±6.7	212±6.8	96.1±9.5	**36.4±7**	76.2±8.2	141.5±11.9	**190.5±15.5**
		Right	78±6.1	210±5.3	98.4±9.4	**30.6±6.2**	73.6±6.7	138.8±10.2	**182.3±15.9**
		p	0.079	0.16	0.182	**<0.001**	0.06	0.199	**<0.001**
	M(22)	**Left**	77.5±6.4	214.3±10.2	**97.4±11.3**	**36.1±6.1**	75.4±5.1	140.2±14.6	**185.2±15**
		Right	78.3±5.8	212.6±7.8	**102.5±12.5**	**31.6±6.9**	75.8±6.6	140.4±13.8	**176.1±11.8**
		p	0.561	0.172	**<0.01**	**<0.001**	0.701	0.899	**<0.01**
41-50 yr	F(18)	**Left**	**84.4±6**	216.3±7.9	**117±9.7**	**36.3±10**	79.2±10.4	162.7±11.8	**194.1±12.1**
		Right	**88.5±5.5**	216.7±9.9	**123.9±14.6**	**32.9±10.6**	78.8±10.3	159.2±13.9	**184.8±14.1**
		p	**0.013**	0.728	**0.021**	**<0.01**	0.789	0.14	**<0.001**
	M(14)	**Left**	**89.1±7.2**	222.1±11.4	119.6±14.5	**39.2±8**	81.7±8.1	166.5±15.9	**201.8±18.2**
		Right	**93.8±8.9**	223.5±8.8	123.1±12.2	**35.7±9**	83.2±10	165±16.6	**193.7±15.4**
		p	**0.019**	0.257	0.145	**0.01**	0.214	0.646	**<0.01**
51-60 yr	F(24)	**Left**	**91.8±5.9**	**219.3±7.5**	**128.6±12.2**	**33.5±6.4**	**79.3±6.2**	174±18.2	**199.8±14.5**
		Right	**96.7±9**	**223.7±7.5**	**138.4±12.5**	**28.4±5.5**	**77.2±6**	171.3±17.3	**185±17.5**
		p	**<0.01**	**<0.01**	**<0.001**	**<0.001**	**<0.01**	0.195	**<0.001**
	M(21)	**Left**	**95.4±10.2**	222±6.5	**139.7±15.3**	**38.3±8.4**	83±8.1	170±11.7	**203.8±15.1**
		Right	**99.7±7.4**	224±6.7	**146.6±14.1**	**32.7±7.2**	81.6±8.1	168.7±12.4	**190.7±13**
		p	**0.026**	0.212	**<0.001**	**<0.001**	0.09	0.257	**<0.001**
61-70 yr	F(13)	**Left**	100.4±9.7	223±7.9	**148.9±18.7**	**32.6±6.9**	**82.4±8.9**	181.4±9.3	**204.9±9.9**
		Right	103.1±7.5	226.1±7.5	**160.1±18.9**	**28.5±9.9**	**79.7±8.1**	179.6±17.5	**197.2±10.5**
		p	0.244	0.062	**<0.01**	**<0.01**	**<0.01**	0.558	**<0.01**
	M(14)	**Left**	**102.8±11.9**	**225.7±9.3**	**143.8±15.3**	**34.3±6.8**	84±7.1	180.8±16.4	198.7±9.7
		Right	**107.8±10.9**	**231.4±8.2**	**158.3±18**	**29.8±8.5**	85.4±10.4	175.5±11.3	194±12
		p	**0.018**	**<0.01**	**<0.001**	**<0.01**	0.598	0.183	0.167

Bold numbers show significant difference between the two hemispheres. *($p<0.05$)*

APPENDIX C

JOHN WILEY AND SONS LICENSE TERMS AND CONDITIONS

Jul 26, 2016

This Agreement between Kiarash Ghassaban ("You") and John Wiley and Sons ("John Wiley and Sons") consists of your license details and the terms and conditions provided by John Wiley and Sons and Copyright Clearance Center.

License Number	3916590880705
License date	Jul 26, 2016
Licensed Content Publisher	John Wiley and Sons
Licensed Content Publication	Journal of Magnetic Resonance Imaging
Licensed Content Title	Assessing global and regional iron content in deep gray matter as a function of age using susceptibility mapping
Licensed Content Author	Manju Liu,Saifeng Liu,Kiarash Ghassaban,Weili Zheng,Dane Dicicco,Yanwei Miao,Charbel Habib,Tarek Jazmati,E. Mark Haacke
Licensed Content Date	Dec 23, 2015
Licensed Content Pages	13
Type of use	Dissertation/Thesis
Requestor type	Author of this Wiley article
Format	Print and electronic
Portion	Full article
Will you be translating?	No
Title of your thesis / dissertation	Quantitative Assessment of Brain Iron Content as a Function of Age using Magnetic Resonance Imaging
Expected completion date	Aug 2016
Expected size (number of pages)	120
Requestor Location	
Publisher Tax ID	EU826007151
Billing Type	Invoice
Billing Address	
Total	0.00 USD
Terms and Conditions	

TERMS AND CONDITIONS

This copyrighted material is owned by or exclusively licensed to John Wiley & Sons, Inc. or one of its group companies (each a"Wiley Company") or handled on behalf of a society with which a Wiley Company has exclusive publishing rights in relation to a particular work (collectively "WILEY"). By clicking "accept" in connection with completing this licensing transaction, you agree that the following terms and conditions apply to this transaction (along with the billing and payment terms and conditions established by the Copyright Clearance Center Inc., ("CCC's Billing and Payment terms and conditions"), at the time that you opened your RightsLink account (these are available at any time at http://myaccount.copyright.com).

Terms and Conditions

- The materials you have requested permission to reproduce or reuse (the "Wiley Materials") are protected by copyright.

- You are hereby granted a personal, non-exclusive, non-sub licensable (on a stand-alone basis), non-transferable, worldwide, limited license to reproduce the Wiley Materials for the purpose specified in the licensing process. This license, **and any CONTENT (PDF or image file) purchased as part of your order,** is for a one-time use only and limited to any maximum distribution number specified in the license. The first instance of republication or reuse granted by this license must be completed within two years of the date of the grant of this license (although copies prepared before the end date may be distributed thereafter). The Wiley Materials shall not be used in any other manner or for any other purpose, beyond what is granted in the license. Permission is granted subject to an appropriate acknowledgement given to the author, title of the material/book/journal and the publisher. You shall also duplicate the copyright notice that appears in the Wiley publication in your use of the Wiley Material. Permission is also granted on the understanding that nowhere in the text is a previously published source acknowledged for all or part of this Wiley Material. Any third party content is expressly excluded from this permission.

- With respect to the Wiley Materials, all rights are reserved. Except as expressly granted by the terms of the license, no part of the Wiley Materials may be copied, modified, adapted (except for minor reformatting required by the new Publication), translated, reproduced, transferred or distributed, in any form or by any means, and no derivative works may be made based on the Wiley Materials without the prior permission of the respective copyright owner.**For STM Signatory Publishers clearing permission under the terms of the STM Permissions Guidelines only, the terms of the license are extended to include subsequent editions and for editions in other languages, provided such editions are for the work as a whole in situ and does not involve the separate exploitation of the permitted figures or extracts,** You may not alter, remove or suppress in any manner any copyright, trademark or other notices displayed by the Wiley Materials. You may not license, rent, sell, loan, lease, pledge, offer as security, transfer or assign the Wiley Materials on a stand-alone basis, or any of the rights granted to you hereunder to any other person.

- The Wiley Materials and all of the intellectual property rights therein shall at all times remain the exclusive property of John Wiley & Sons Inc, the Wiley Companies, or their respective licensors, and your interest therein is only that of having possession of and the right to reproduce the Wiley Materials pursuant to Section 2 herein during the continuance of this Agreement. You agree that you own no right, title or interest in or to the Wiley Materials or any of the intellectual property rights therein. You shall have no rights hereunder other than the license as provided for above in Section 2. No right, license or interest to any trademark, trade name, service mark or other branding

("Marks") of WILEY or its licensors is granted hereunder, and you agree that you shall not assert any such right, license or interest with respect thereto

- NEITHER WILEY NOR ITS LICENSORS MAKES ANY WARRANTY OR REPRESENTATION OF ANY KIND TO YOU OR ANY THIRD PARTY, EXPRESS, IMPLIED OR STATUTORY, WITH RESPECT TO THE MATERIALS OR THE ACCURACY OF ANY INFORMATION CONTAINED IN THE MATERIALS, INCLUDING, WITHOUT LIMITATION, ANY IMPLIED WARRANTY OF MERCHANTABILITY, ACCURACY, SATISFACTORY QUALITY, FITNESS FOR A PARTICULAR PURPOSE, USABILITY, INTEGRATION OR NON-INFRINGEMENT AND ALL SUCH WARRANTIES ARE HEREBY EXCLUDED BY WILEY AND ITS LICENSORS AND WAIVED BY YOU.

- WILEY shall have the right to terminate this Agreement immediately upon breach of this Agreement by you.

- You shall indemnify, defend and hold harmless WILEY, its Licensors and their respective directors, officers, agents and employees, from and against any actual or threatened claims, demands, causes of action or proceedings arising from any breach of this Agreement by you.

- IN NO EVENT SHALL WILEY OR ITS LICENSORS BE LIABLE TO YOU OR ANY OTHER PARTY OR ANY OTHER PERSON OR ENTITY FOR ANY SPECIAL, CONSEQUENTIAL, INCIDENTAL, INDIRECT, EXEMPLARY OR PUNITIVE DAMAGES, HOWEVER CAUSED, ARISING OUT OF OR IN CONNECTION WITH THE DOWNLOADING, PROVISIONING, VIEWING OR USE OF THE MATERIALS REGARDLESS OF THE FORM OF ACTION, WHETHER FOR BREACH OF CONTRACT, BREACH OF WARRANTY, TORT, NEGLIGENCE, INFRINGEMENT OR OTHERWISE (INCLUDING, WITHOUT LIMITATION, DAMAGES BASED ON LOSS OF PROFITS, DATA, FILES, USE, BUSINESS OPPORTUNITY OR CLAIMS OF THIRD PARTIES), AND WHETHER OR NOT THE PARTY HAS BEEN ADVISED OF THE POSSIBILITY OF SUCH DAMAGES. THIS LIMITATION SHALL APPLY NOTWITHSTANDING ANY FAILURE OF ESSENTIAL PURPOSE OF ANY LIMITED REMEDY PROVIDED HEREIN.

- Should any provision of this Agreement be held by a court of competent jurisdiction to be illegal, invalid, or unenforceable, that provision shall be deemed amended to achieve as nearly as possible the same economic effect as the original provision, and the legality, validity and enforceability of the remaining provisions of this Agreement shall not be affected or impaired thereby.

- The failure of either party to enforce any term or condition of this Agreement shall not constitute a waiver of either party's right to enforce each and every term and condition of this Agreement. No breach under this agreement shall be deemed waived or excused by either party unless such waiver or consent is in writing signed by the party granting such waiver or consent. The waiver by or consent of a party to a breach of any provision of this Agreement shall not operate or be construed as a waiver of or consent to any other or subsequent breach by such other party.

- This Agreement may not be assigned (including by operation of law or otherwise) by you without WILEY's prior written consent.

- Any fee required for this permission shall be non-refundable after thirty (30) days from receipt by the CCC.
- These terms and conditions together with CCC's Billing and Payment terms and conditions (which are incorporated herein) form the entire agreement between you and WILEY concerning this licensing transaction and (in the absence of fraud) supersedes all prior agreements and representations of the parties, oral or written. This Agreement may not be amended except in writing signed by both parties. This Agreement shall be binding upon and inure to the benefit of the parties' successors, legal representatives, and authorized assigns.
- In the event of any conflict between your obligations established by these terms and conditions and those established by CCC's Billing and Payment terms and conditions, these terms and conditions shall prevail.
- WILEY expressly reserves all rights not specifically granted in the combination of (i) the license details provided by you and accepted in the course of this licensing transaction, (ii) these terms and conditions and (iii) CCC's Billing and Payment terms and conditions.
- This Agreement will be void if the Type of Use, Format, Circulation, or Requestor Type was misrepresented during the licensing process.
- This Agreement shall be governed by and construed in accordance with the laws of the State of New York, USA, without regards to such state's conflict of law rules. Any legal action, suit or proceeding arising out of or relating to these Terms and Conditions or the breach thereof shall be instituted in a court of competent jurisdiction in New York County in the State of New York in the United States of America and each party hereby consents and submits to the personal jurisdiction of such court, waives any objection to venue in such court and consents to service of process by registered or certified mail, return receipt requested, at the last known address of such party.

WILEY OPEN ACCESS TERMS AND CONDITIONS

Wiley Publishes Open Access Articles in fully Open Access Journals and in Subscription journals offering Online Open. Although most of the fully Open Access journals publish open access articles under the terms of the Creative Commons Attribution (CC BY) License only, the subscription journals and a few of the Open Access Journals offer a choice of Creative Commons Licenses. The license type is clearly identified on the article.

The Creative Commons Attribution License

The Creative Commons Attribution License (CC-BY) allows users to copy, distribute and transmit an article, adapt the article and make commercial use of the article. The CC-BY license permits commercial and non-

Creative Commons Attribution Non-Commercial License

The Creative Commons Attribution Non-Commercial (CC-BY-NC)License permits use, distribution and reproduction in any medium, provided the original work is properly cited and is not used for commercial purposes.(see below)

Creative Commons Attribution-Non-Commercial-NoDerivs License

The Creative Commons Attribution Non-Commercial-NoDerivs License (CC-BY-NC-ND) permits use, distribution and reproduction in any medium, provided the original work is properly cited, is not used for commercial purposes and no modifications or adaptations are made. (see below)

Use by commercial "for-profit" organizations

Use of Wiley Open Access articles for commercial, promotional, or marketing purposes requires further explicit permission from Wiley and will be subject to a fee.
Further details can be found on Wiley Online Library
http://olabout.wiley.com/WileyCDA/Section/id-410895.html

Other Terms and Conditions:

v1.10 Last updated September 2015

Questions? customercare@copyright.com or +1-855-239-3415 (toll free in the US) or +1-978-646-2777.

REFERENCES

Abdul-Rahman, H. S., M. A. Gdeisat, D. R. Burton, M. J. Lalor, F. Lilley, and C. J. Moore. 2007. 'Fast and robust three-dimensional best path phase unwrapping algorithm', *Appl Opt*, 46: 6623-35.

Acosta-Cabronero, J., M. J. Betts, A. Cardenas-Blanco, S. Yang, and P. J. Nestor. 2016. 'In Vivo MRI Mapping of Brain Iron Deposition across the Adult Lifespan', *J Neurosci*, 36: 364-74.

Adin, M. E., L. Kleinberg, D. Vaidya, E. Zan, S. Mirbagheri, and D. M. Yousem. 2015. 'Hyperintense Dentate Nuclei on T1-Weighted MRI: Relation to Repeat Gadolinium Administration', *AJNR Am J Neuroradiol*, 36: 1859-65.

Antharam, V., J. F. Collingwood, J. P. Bullivant, M. R. Davidson, S. Chandra, A. Mikhaylova, M. E. Finnegan, C. Batich, J. R. Forder, and J. Dobson. 2012. 'High field magnetic resonance microscopy of the human hippocampus in Alzheimer's disease: quantitative imaging and correlation with iron', *Neuroimage*, 59: 1249-60.

Aquino, D., A. Bizzi, M. Grisoli, B. Garavaglia, M. G. Bruzzone, N. Nardocci, M. Savoiardo, and L. Chiapparini. 2009. 'Age-related iron deposition in the basal ganglia: quantitative analysis in healthy subjects', *Radiology*, 252: 165-72.

Ayton, S., P. Lei, J. A. Duce, B. X. Wong, A. Sedjahtera, P. A. Adlard, A. I. Bush, and D. I. Finkelstein. 2013. 'Ceruloplasmin dysfunction and therapeutic potential for Parkinson disease', *Ann Neurol*, 73: 554-9.

Baraibar, M. A., A. G. Barbeito, B. B. Muhoberac, and R. Vidal. 2008. 'Iron-mediated aggregation and a localized structural change characterize ferritin from a mutant light chain polypeptide that causes neurodegeneration', *J Biol Chem*, 283: 31679-89.

Barbosa, J. H., A. C. Santos, V. Tumas, M. Liu, W. Zheng, E. M. Haacke, and C. E. Salmon. 2015. 'Quantifying brain iron deposition in patients with Parkinson's disease using quantitative susceptibility mapping, R2 and R2', *Magn Reson Imaging*, 33: 559-65.

Beard, J. 2003. 'Iron deficiency alters brain development and functioning', *J Nutr*, 133: 1468S-72S.

Benson, R. R., R. Gattu, B. Sewick, Z. Kou, N. Zakariah, J. M. Cavanaugh, and E. M. Haacke. 2012. 'Detection of hemorrhagic and axonal pathology in mild traumatic brain injury using advanced MRI: implications for neurorehabilitation', *NeuroRehabilitation*, 31: 261-79.

Berg, D., and M. B. Youdim. 2006. 'Role of iron in neurodegenerative disorders', *Top Magn Reson Imaging*, 17: 5-17.

Bilgic, B., A. Pfefferbaum, T. Rohlfing, E. V. Sullivan, and E. Adalsteinsson. 2012. 'MRI estimates of brain iron concentration in normal aging using quantitative susceptibility mapping', *Neuroimage*, 59: 2625-35.

Bonilha da Silva, C., F. P. Bergo, A. D'Abreu, F. Cendes, I. Lopes-Cendes, and M. C. Franca, Jr. 2014. 'Dentate nuclei T2 relaxometry is a reliable neuroimaging marker in Friedreich's ataxia', *Eur J Neurol*, 21: 1131-6.

Cherubini, A., P. Peran, C. Caltagirone, U. Sabatini, and G. Spalletta. 2009. 'Aging of subcortical nuclei: microstructural, mineralization and atrophy modifications measured in vivo using MRI', *Neuroimage*, 48: 29-36.

Connor, J. R., B. S. Snyder, J. L. Beard, R. E. Fine, and E. J. Mufson. 1992. 'Regional distribution of iron and iron-regulatory proteins in the brain in aging and Alzheimer's disease', *J Neurosci Res*, 31: 327-35.

Cortese, S., E. Konofal, B. D. Bernardina, M. C. Mouren, and M. Lecendreux. 2009. 'Sleep disturbances and serum ferritin levels in children with attention-deficit/hyperactivity disorder', *Eur Child Adolesc Psychiatry*, 18: 393-9.

Deistung, A., A. Schafer, F. Schweser, U. Biedermann, R. Turner, and J. R. Reichenbach. 2013. 'Toward in vivo histology: a comparison of quantitative susceptibility mapping (QSM) with magnitude-, phase-, and R2*-imaging at ultra-high magnetic field strength', *Neuroimage*, 65: 299-314.

Deville, G. , M. Bernier, and J. M. Delrieux. 1979. 'NMR multiple echoes observed in solid 3He', *Physical Review B*, 19: 5666-88.

Du, S., S. K. Sah, C. Zeng, J. Wang, Y. Liu, H. Xiong, and Y. Li. 2015. 'Iron deposition in the gray matter in patients with relapse-remitting multiple sclerosis: A longitudinal study using three-dimensional (3D)-enhanced T2*-weighted angiography (ESWAN)', *Eur J Radiol*, 84: 1325-32.

Gomes, J. A., M. Selim, A. Cotleur, M. S. Hussain, G. Toth, L. Koffman, K. Asi, and J. J. Provencio. 2014. 'Brain Iron Metabolism and Brain Injury Following Subarachnoid Hemorrhage: iCeFISH-Pilot (CSF Iron in SAH)', *Neurocrit Care*.

Haacke, E. M., M. Ayaz, A. Khan, E. S. Manova, B. Krishnamurthy, L. Gollapalli, C. Ciulla, I. Kim, F. Petersen, and W. Kirsch. 2007. 'Establishing a baseline phase behavior in magnetic resonance imaging to determine normal vs. abnormal iron content in the brain', *J Magn Reson Imaging*, 26: 256-64.

Haacke, E. M., N. Y. Cheng, M. J. House, Q. Liu, J. Neelavalli, R. J. Ogg, A. Khan, M. Ayaz, W. Kirsch, and A. Obenaus. 2005. 'Imaging iron stores in the brain using magnetic resonance imaging', *Magn Reson Imaging*, 23: 1-25.

Haacke, E. M., S. Liu, S. Buch, W. Zheng, D. Wu, and Y. Ye. 2015. 'Quantitative susceptibility mapping: current status and future directions', *Magn Reson Imaging*, 33: 1-25.

Haacke, E. M., Y. Miao, M. Liu, C. A. Habib, Y. Katkuri, T. Liu, Z. Yang, Z. Lang, J. Hu, and J. Wu. 2010. 'Correlation of putative iron content as represented by changes in R2* and phase with age in deep gray matter of healthy adults', *J Magn Reson Imaging*, 32: 561-76.

Haacke, E. M., J. Tang, J. Neelavalli, and Y. C. Cheng. 2010. 'Susceptibility mapping as a means to visualize veins and quantify oxygen saturation', *J Magn Reson Imaging*, 32: 663-76.

Haacke, E. M., Y. Xu, Y. C. Cheng, and J. R. Reichenbach. 2004. 'Susceptibility weighted imaging (SWI)', *Magn Reson Med*, 52: 612-8.

Haacke, E. Mark. 1999. *Magnetic resonance imaging : physical principles and sequence design* (Wiley: New York).

Haacke, E. Mark, Jürgen R. Reichenbach, and ebrary Inc. 2011. "Susceptibility weighted imaging in MRI basic concepts and clinical applications." In, xvi, 743 p. Hoboken, N.J.: Wiley-Blackwell,.

Habib, C. A., M. Liu, N. Bawany, J. Garbern, I. Krumbein, H. J. Mentzel, J. Reichenbach, C. Magnano, R. Zivadinov, and E. M. Haacke. 2012. 'Assessing abnormal iron content in the deep gray matter of patients with multiple sclerosis versus healthy controls', *AJNR Am J Neuroradiol*, 33: 252-8.

Hallgren, B., and P. Sourander. 1958. 'The effect of age on the non-haemin iron in the human brain', *J Neurochem*, 3: 41-51.

Hare, D., S. Ayton, A. Bush, and P. Lei. 2013. 'A delicate balance: Iron metabolism and diseases of the brain', *Front Aging Neurosci*, 5: 34.

He, N., P. Huang, H. Ling, J. Langley, C. Liu, B. Ding, J. Huang, H. Xu, Y. Zhang, Z. Zhang, X. Hu, S. Chen, and F. Yan. 2016. 'Dentate nucleus iron deposition is a potential biomarker for tremor-dominant Parkinson's disease', *NMR Biomed*.

Hu, H. H., A. Pokorney, R. B. Towbin, and J. H. Miller. 2016. 'Increased signal intensities in the dentate nucleus and globus pallidus on unenhanced T1-weighted images: evidence in children undergoing multiple gadolinium MRI exams', *Pediatr Radiol*.

Jeong, S. Y., D. R. Crooks, H. Wilson-Ollivierre, M. C. Ghosh, R. Sougrat, J. Lee, S. Cooperman, J. B. Mitchell, C. Beaumont, and T. A. Rouault. 2011. 'Iron insufficiency compromises motor neurons and their mitochondrial function in Irp2-null mice', *PLoS One*, 6: e25404.

Kanda, T., K. Ishii, H. Kawaguchi, K. Kitajima, and D. Takenaka. 2014. 'High signal intensity in the dentate nucleus and globus pallidus on unenhanced T1-weighted MR images: relationship

with increasing cumulative dose of a gadolinium-based contrast material', *Radiology*, 270: 834-41.

Kanda, T., H. Oba, K. Toyoda, and S. Furui. 2016. 'Macrocyclic Gadolinium-Based Contrast Agents Do Not Cause Hyperintensity in the Dentate Nucleus', *AJNR Am J Neuroradiol*, 37: E41.

Kanda, T., H. Oba, K. Toyoda, K. Kitajima, and S. Furui. 2016. 'Brain gadolinium deposition after administration of gadolinium-based contrast agents', *Jpn J Radiol*, 34: 3-9.

Khadilkar, S., S. Jaggi, B. Patel, R. Yadav, P. Hanagandi, and L. L. Faria do Amaral. 2016. 'A practical approach to diseases affecting dentate nuclei', *Clin Radiol*, 71: 107-19.

Khalil, M., C. Langkammer, S. Ropele, K. Petrovic, M. Wallner-Blazek, M. Loitfelder, M. Jehna, G. Bachmaier, R. Schmidt, C. Enzinger, S. Fuchs, and F. Fazekas. 2011. 'Determinants of brain iron in multiple sclerosis: a quantitative 3T MRI study', *Neurology*, 77: 1691-7.

Kleinig, T. J. 2013. 'Associations and implications of cerebral microbleeds', *J Clin Neurosci*, 20: 919-27.

Langkammer, C., N. Krebs, W. Goessler, E. Scheurer, F. Ebner, K. Yen, F. Fazekas, and S. Ropele. 2010. 'Quantitative MR imaging of brain iron: a postmortem validation study', *Radiology*, 257: 455-62.

Langkammer, C., N. Krebs, W. Goessler, E. Scheurer, K. Yen, F. Fazekas, and S. Ropele. 2012. 'Susceptibility induced gray-white matter MRI contrast in the human brain', *Neuroimage*, 59: 1413-9.

Langkammer, C., S. Ropele, L. Pirpamer, F. Fazekas, and R. Schmidt. 2014. 'MRI for iron mapping in Alzheimer's disease', *Neurodegener Dis*, 13: 189-91.

Langkammer, C., F. Schweser, N. Krebs, A. Deistung, W. Goessler, E. Scheurer, K. Sommer, G. Reishofer, K. Yen, F. Fazekas, S. Ropele, and J. R. Reichenbach. 2012. 'Quantitative susceptibility mapping (QSM) as a means to measure brain iron? A post mortem validation study', *Neuroimage*, 62: 1593-9.

Li, W., B. Wu, A. Batrachenko, V. Bancroft-Wu, R. A. Morey, V. Shashi, C. Langkammer, M. D. De Bellis, S. Ropele, A. W. Song, and C. Liu. 2014. 'Differential developmental trajectories of magnetic susceptibility in human brain gray and white matter over the lifespan', *Hum Brain Mapp*, 35: 2698-713.

Li, W., B. Wu, and C. Liu. 2011. 'Quantitative susceptibility mapping of human brain reflects spatial variation in tissue composition', *Neuroimage*, 55: 1645-56.

Lim, I. A., A. V. Faria, X. Li, J. T. Hsu, R. D. Airan, S. Mori, and P. C. van Zijl. 2013. 'Human brain atlas for automated region of interest selection in quantitative susceptibility mapping: application to determine iron content in deep gray matter structures', *Neuroimage*, 82: 449-69.

Liu, Saifeng. 2014. 'Technical Improvements in Quantitative Susceptibility Mapping', McMaster University.

Liu, T., P. Spincemaille, L. de Rochefort, B. Kressler, and Y. Wang. 2009. 'Calculation of susceptibility through multiple orientation sampling (COSMOS): a method for conditioning the inverse problem from measured magnetic field map to susceptibility source image in MRI', *Magn Reson Med*, 61: 196-204.

Loef, M., and H. Walach. 2012. 'Copper and iron in Alzheimer's disease: a systematic review and its dietary implications', *Br J Nutr*, 107: 7-19.

Maschke, M., J. Weber, A. Dimitrova, U. Bonnet, J. Bohrenkamper, S. Sturm, K. Kindsvater, B. W. Muller, M. Gastpar, H. C. Diener, M. Forsting, and D. Timmann. 2004. 'Age-related changes of the dentate nuclei in normal adults as revealed by 3D fast low angle shot (FLASH) echo sequence magnetic resonance imaging', *J Neurol*, 251: 740-6.

Miller, J. H., H. H. Hu, A. Pokorney, P. Cornejo, and R. Towbin. 2015. 'MRI Brain Signal Intensity Changes of a Child During the Course of 35 Gadolinium Contrast Examinations', *Pediatrics*, 136: e1637-40.

Mitsumori, F., H. Watanabe, and N. Takaya. 2009. 'Estimation of brain iron concentration in vivo using a linear relationship between regional iron and apparent transverse relaxation rate of the tissue water at 4.7T', *Magn Reson Med*, 62: 1326-30.

Novellino, F., A. Cherubini, C. Chiriaco, M. Morelli, M. Salsone, G. Arabia, and A. Quattrone. 2013. 'Brain iron deposition in essential tremor: a quantitative 3-Tesla magnetic resonance imaging study', *Mov Disord*, 28: 196-200.

Peran, P., A. Cherubini, G. Luccichenti, G. Hagberg, J. F. Demonet, O. Rascol, P. Celsis, C. Caltagirone, G. Spalletta, and U. Sabatini. 2009. 'Volume and iron content in basal ganglia and thalamus', *Hum Brain Mapp*, 30: 2667-75.

Persson, N., J. Wu, Q. Zhang, T. Liu, J. Shen, R. Bao, M. Ni, T. Liu, Y. Wang, and P. Spincemaille. 2015. 'Age and sex related differences in subcortical brain iron concentrations among healthy adults', *Neuroimage*, 122: 385-98.

Pfefferbaum, A., E. Adalsteinsson, T. Rohlfing, and E. V. Sullivan. 2009. 'MRI estimates of brain iron concentration in normal aging: comparison of field-dependent (FDRI) and phase (SWI) methods', *Neuroimage*, 47: 493-500.

Popescu, B. F., M. J. George, U. Bergmann, A. V. Garachtchenko, M. E. Kelly, R. P. McCrea, K. Luning, R. M. Devon, G. N. George, A. D. Hanson, S. M. Harder, L. D. Chapman, I. J. Pickering, and H. Nichol. 2009. 'Mapping metals in Parkinson's and normal brain using rapid-scanning x-ray fluorescence', *Phys Med Biol*, 54: 651-63.

Ramalho, J., R. C. Semelka, M. AlObaidy, M. Ramalho, R. H. Nunes, and M. Castillo. 2016. 'Signal intensity change on unenhanced T1-weighted images in dentate nucleus following gadobenate dimeglumine in patients with and without previous multiple administrations of gadodiamide', *Eur Radiol*.

Reichenbach, J. R., F. Schweser, B. Serres, and A. Deistung. 2015. 'Quantitative Susceptibility Mapping: Concepts and Applications', *Clin Neuroradiol*, 25 Suppl 2: 225-30.

Reichenbach, J. R., R. Venkatesan, D. A. Yablonskiy, M. R. Thompson, S. Lai, and E. M. Haacke. 1997. 'Theory and application of static field inhomogeneity effects in gradient-echo imaging', *J Magn Reson Imaging*, 7: 266-79.

Roberts, D. R., and K. R. Holden. 2016. 'Progressive increase of T1 signal intensity in the dentate nucleus and globus pallidus on unenhanced T1-weighted MR images in the pediatric brain exposed to multiple doses of gadolinium contrast', *Brain Dev*, 38: 331-6.

Ropele, S., W. de Graaf, M. Khalil, M. P. Wattjes, C. Langkammer, M. A. Rocca, A. Rovira, J. Palace, F. Barkhof, M. Filippi, and F. Fazekas. 2011. 'MRI assessment of iron deposition in multiple sclerosis', *J Magn Reson Imaging*, 34: 13-21.

Rosas, H. D., Y. I. Chen, G. Doros, D. H. Salat, N. K. Chen, K. K. Kwong, A. Bush, J. Fox, and S. M. Hersch. 2012. 'Alterations in brain transition metals in Huntington disease: an evolving and intricate story', *Arch Neurol*, 69: 887-93.

Saab, C. Y., and W. D. Willis. 2003. 'The cerebellum: organization, functions and its role in nociception', *Brain Res Brain Res Rev*, 42: 85-95.

Schenck, J. F., and E. A. Zimmerman. 2004. 'High-field magnetic resonance imaging of brain iron: birth of a biomarker?', *NMR Biomed*, 17: 433-45.

Schweser, F., A. Deistung, B. W. Lehr, and J. R. Reichenbach. 2011. 'Quantitative imaging of intrinsic magnetic tissue properties using MRI signal phase: an approach to in vivo brain iron metabolism?', *Neuroimage*, 54: 2789-807.

Shmueli, K., J. A. de Zwart, P. van Gelderen, T. Q. Li, S. J. Dodd, and J. H. Duyn. 2009. 'Magnetic susceptibility mapping of brain tissue in vivo using MRI phase data', *Magn Reson Med*, 62: 1510-22.

Smith, S. M. 2002. 'Fast robust automated brain extraction', *Hum Brain Mapp*, 17: 143-55.

Solbach, K., O. Kraff, M. Minnerop, A. Beck, L. Schols, E. R. Gizewski, M. E. Ladd, and D. Timmann. 2014. 'Cerebellar pathology in Friedreich's ataxia: atrophied dentate nuclei with normal iron content', *Neuroimage Clin*, 6: 93-9.

Stankiewicz, J., S. S. Panter, M. Neema, A. Arora, C. E. Batt, and R. Bakshi. 2007. 'Iron in chronic brain disorders: imaging and neurotherapeutic implications', *Neurotherapeutics*, 4: 371-86.

Stojanov, D. A., A. Aracki-Trenkic, S. Vojinovic, D. Benedeto-Stojanov, and S. Ljubisavljevic. 2016. 'Increasing signal intensity within the dentate nucleus and globus pallidus on unenhanced T1W magnetic resonance images in patients with relapsing-remitting multiple sclerosis: correlation with cumulative dose of a macrocyclic gadolinium-based contrast agent, gadobutrol', *Eur Radiol*, 26: 807-15.

Stojanov, D., A. Aracki-Trenkic, and D. Benedeto-Stojanov. 2016. 'Gadolinium deposition within the dentate nucleus and globus pallidus after repeated administrations of gadolinium-based contrast agents-current status', *Neuroradiology*, 58: 433-41.

Stuber, C., M. Morawski, A. Schafer, C. Labadie, M. Wahnert, C. Leuze, M. Streicher, N. Barapatre, K. Reimann, S. Geyer, D. Spemann, and R. Turner. 2014. 'Myelin and iron concentration in the human brain: a quantitative study of MRI contrast', *Neuroimage*, 93 Pt 1: 95-106.

Sultan, F., S. Hamodeh, and J. S. Baizer. 2010. 'The human dentate nucleus: a complex shape untangled', *Neuroscience*, 167: 965-8.

Sun, H., A. J. Walsh, R. M. Lebel, G. Blevins, I. Catz, J. Q. Lu, E. S. Johnson, D. J. Emery, K. G. Warren, and A. H. Wilman. 2015. 'Validation of quantitative susceptibility mapping with Perls' iron staining for subcortical gray matter', *Neuroimage*, 105: 486-92.

Tang, J., S. Liu, J. Neelavalli, Y. C. Cheng, S. Buch, and E. M. Haacke. 2013. 'Improving susceptibility mapping using a threshold-based K-space/image domain iterative reconstruction approach', *Magn Reson Med*, 69: 1396-407.

Tedeschi, E., G. Palma, A. Canna, S. Cocozza, C. Russo, P. Borrelli, R. Lanzillo, V. Angelini, E. Postiglione, V. B. Morra, M. Salvatore, A. Brunetti, and M. Quarantelli. 2016. 'In vivo dentate nucleus MRI relaxometry correlates with previous administration of Gadolinium-based contrast agents', *Eur Radiol*.

Udipi, Shobha , Padmini Ghugre, and Chanda Gokhale. 2012. 'Iron, Oxidative Stress and Health.' in Volodymyr Lushchak (ed.), *Oxidative Stress - Molecular Mechanisms and Biological Effects* (InTech).

Wang, Y., Y. Yu, D. Li, K. T. Bae, J. J. Brown, W. Lin, and E. M. Haacke. 2000. 'Artery and vein separation using susceptibility-dependent phase in contrast-enhanced MRA', *J Magn Reson Imaging*, 12: 661-70.

Wharton, S., and R. Bowtell. 2010. 'Whole-brain susceptibility mapping at high field: a comparison of multiple- and single-orientation methods', *Neuroimage*, 53: 515-25.

Xu, X., Q. Wang, and M. Zhang. 2008. 'Age, gender, and hemispheric differences in iron deposition in the human brain: an in vivo MRI study', *Neuroimage*, 40: 35-42.

Yao, B., T. Q. Li, Pv Gelderen, K. Shmueli, J. A. de Zwart, and J. H. Duyn. 2009. 'Susceptibility contrast in high field MRI of human brain as a function of tissue iron content', *Neuroimage*, 44: 1259-66.

Zheng, W., H. Nichol, S. Liu, Y. C. Cheng, and E. M. Haacke. 2013. 'Measuring iron in the brain using quantitative susceptibility mapping and X-ray fluorescence imaging', *Neuroimage*, 78: 68-74.

Zivadinov, R., C. Schirda, M. G. Dwyer, M. E. Haacke, B. Weinstock-Guttman, E. Menegatti, M. Heininen-Brown, C. Magnano, A. M. Malagoni, D. S. Wack, D. Hojnacki, C. Kennedy, E. Carl, N. Bergsland, S. Hussein, G. Poloni, I. Bartolomei, F. Salvi, and P. Zamboni. 2010. 'Chronic cerebrospinal venous insufficiency and iron deposition on susceptibility-weighted imaging in patients with multiple sclerosis: a pilot case-control study', *Int Angiol*, 29: 158-75.

ABSTRACT

QUANTITATIVE ASSESSMENT OF BRAIN IRON CONTENT AS A FUNCTION OF AGE USING MAGNETIC RESONANCE IMAGING

by

KIARASH GHASSABAN

August 2016

Advisor: Prof. E. Mark Haacke

Major: Biomedical Engineering

Degree: Master of Science

As the most abundant transition metal in the brain, iron is known to play a key role in a variety of functional and cellular processes. Recent *in vivo* and post-mortem studies have shown that the levels of iron deposition in the brain, particularly in deep gray matter nuclei, vary as a function of age. On the other hand, elevated iron has also been associated with some neurodegenerative diseases such as Multiple Sclerosis (MS) and Parkinson's disease (PD) among others.

Magnetic Resonance Imaging (MRI) is a widely used non-invasive and non-ionizing imaging modality which is sensitive to magnetic properties of materials through their magnetic susceptibilities. This makes it particularly useful in imaging as iron (which is paramagnetic) and calcium (which is diamagnetic). Recent developments in magnetic susceptibility mapping have made it possible to track iron changes in the brain. In this thesis, Quantitative Susceptibility Mapping (QSM) is used to establish a baseline of iron content in the basal ganglia, midbrain, and

cerebellar major nuclei as a function of age in healthy controls using both global (whole 3D structural region) and regional (high iron content region) analyses.

In agreement with previous studies, we found that in the global analysis a positive linear susceptibility-age correlation was observed in the putamen, caudate nucleus, and red nucleus while the susceptibility distributions across the lifespan were quite scattered in the globus pallidus, substantia nigra, thalamus, pulvinar thalamus and dentate nucleus. All structures, with the exception of the thalamus, showed increasing susceptibility trend as a function of age in the whole-region analysis. However, in the high iron content region, strong and considerably less scattered correlations were shown between age and magnetic susceptibility in most of the structures, except for the thalamus. These sensitive and robust regional susceptibility-age correlations have the potential to be utilized as a new baseline to investigate abnormal iron content in neurological diseases.

AUTOBIOGRAPHICAL STATEMENT

Kiarash Ghassaban

14487 E 12 Mile Rd, Apt A, Warren, MI 48088 Tel: (313) 909-4143 email: fr2988@wayne.edu

Education

2014-2016	**Master of Science (M.Sc)** in Biomedical Engineering Wayne State University Detroit, MI
2009-2014	**Bachelor of Science (B.Sc)** in Electrical Engineering Amirkabir University of Technology (Tehran Polytechnic) Tehran, Iran
2009-2013	**Bachelor of Science (B.Sc)** in Biomedical Engineering Amirkabir University of Technology (Tehran Polytechnic) Tehran, Iran

Professional Experience

2015-2016	**Graduate Research Assistant** Department of Biomedical Engineering Wayne State University, Detroit, MI
Summer 2015	**Student Assistant** Department of Radiology, School of Medicine Wayne State University, Detroit, MI
2014-2015	**Graduate Research Assistant** Department of Biomedical Engineering Wayne State University, Detroit, MI

Publications

Liu, M., S. Liu, **K. Ghassaban**, W. Zheng, D. Dicicco, Y. Miao, C. Habib, T. Jazmati, and E. M. Haacke. 2016. 'Assessing global and regional iron content in deep gray matter as a function of age using susceptibility mapping', *J Magn Reson Imaging*, 44: 59-71.

K. Ghassaban, M. Liu, C. Habib, and E. Mark Haacke. 2016. 'Establishing a new susceptibility-age baseline to assess iron content in basal ganglia and midbrain nuclei of healthy adults', *American Society of Neuroradiology (ASNR),* Washington D.C.